LRP 726/02 July 2002

Papers presented at the

**12th Joint Workshop on**
**Electron Cyclotron Emission and**
**Electron Cyclotron Resonance Heating**

Aix-en-Provence, France
May 13-16, 2002

*These papers can be found on the following web sites :*

http://crppwww/

*and*

wshop.free.fr/ec12/PAPERS/

ISSN 0458-5895

LIST OF CONTENTS


| | | Page |
|---|---|---|
| - | FULLY OFF-AXIS ECCD DRIVEN PLASMAS IN TCV<br>**Invited paper**<br>*P. Nikkola, O. Sauter, R. Behn, S. Coda, I. Condrea, T.P. Goodman, M.A. Henderson, R.W. Harvey, Y. Peysson, and the TCV team* | 1 |
| - | RADIAL TRANSPORT EFFECTS ON ECCD IN THE TCV AND DIII-D TOKAMAKS AND ON OHMIC DISCHARGES IN THE MST RFP<br>*R.W. Harvey, O. Sauter, R. Prater, P. Nikkola, R .O'Connell, and C.B. Forest* | 11 |
| - | CURRENT PROFILE TAILORING WITH FAR OFF-AXIS ECH POWER DEPOSITION IN TCV ELONGATION EXPERIMENTS<br>*Y. Camenen, A. Pochelon, F. Hofmann, C. Angioni, T.P. Goodman, M.A. Henderson, P. Nikkola, L. Porte, and O. Sauter* | 17 |
| - | EXPLOITATION OF A DIAMAGNETIC LOOP FOR MODULATED ECH POWER ABSORPTION MEASUREMENTS IN TCV<br>*A. Manini, J.-M. Moret, S. Alberti, T.P.Goodman, and M.A. Henderson* | 23 |
| - | PRELIMINARY RESULTS OF TOP LAUNCH 3rd HARMONIC X-MODE ELECTRON CYCLOTRON HEATING IN THE TCV TOKAMAK<br>*J.P. Hogge, S. Alberti, L. Porte, and G. Arnoux* | 29 |

- DESIGN OF THE EVACUATED WAVEGUIDE TRANSMISSION LINES FOR JET-EP 35
*M.A. Henderson, S. Alberti, J. Bird, B. Elzendoorn, T.P. Goodman, F. Hoekzema, G. MacMillan, B. Pioscyk, L. Porte, A.G.A. Verhoeven*

# Fully Off-Axis ECCD Driven Plasmas in TCV

P. Nikkola[1], O. Sauter[1], R. Behn[1], S. Coda[1], I. Condrea[1], T.P. Goodman[1], M.A. Henderson[1], R.W. Harvey[2], Y. Peysson[3], and the TCV team[1]

[1] *Centre de Recherches en Physique des Plasmas, Association Euratom-Confédération Suisse, Ecole Polytechnique Fédérale de Lausanne, CH-1015 Lausanne*

[2] *CompX, P.O. Box 2672, Del Mar, CA 92014-5672, USA*

[3] *DRFC-CEA Cadarache, Aix-en-Provence, France*

Fully non-inductive plasma discharges sustained by off-axis Electron Cyclotron Current Drive (ECCD) in the TCV tokamak are reported. Steady state discharges with very good confinement properties and a large bootstrap current fraction can be created in the absence of an Ohmic field. The total current density profile is hollow owing to the bootstrap current. A steady state electron Internal Transport Barrier (eITB) is observed inside the ECCD deposition radius. Once fully formed, the eITB is efficient in that the addition of 0.45 MW central EC power causes no degradation in the confinement time. Best results are obtained with a small central counter current drive component. In this plasma $H_{RLW} = 4.5$ is reported ($H_{RLW} = \tau_{Ee}/\tau_{RLW}$) with bootstrap current fraction $I_{BS}/I_p = 50\%$. The current profile can be finely tuned at zero loop voltage, allowing operation just below the MHD instability limit. Current density profile modeling is performed with a Fokker-Planck code using a model for radial transport. The bootstrap current is calculated from Thomson profiles.

## 1. Introduction

Recently, very good confinement properties have been obtained in TCV Ohmic plasmas by modifying the current density profile with electron cyclotron resonance heating (ECRH) and electron cyclotron current drive (ECCD) [1,2]. Off-axis ECRH was applied together with central counter current drive (CNT-CD). In these plasmas, confinement enhancement factors, $H_{RLW} = \tau_{Ee}/\tau_{RLW}$, between 3 and 4 have been obtained with electron temperatures in the range of 10 keV. Here, $\tau_{Ee}$ is the experimental electron energy confinement time and $\tau_{RLW}$ is the electron energy confinement time given by the Rebut-Lallia-Watkins scaling (RLW) [3]. The RLW scaling is used as a reference since it has been shown to be a good predictor of TCV confinement in a wide range of Ohmic and ECRH plasmas [4]. These enhanced confinement scenarios are believed to depend on a reversed core magnetic shear and are thus hampered by the rise in on-axis Ohmic current caused by the increase of conductivity with temperature. In this paper it is shown that confinement is improved further in the absence of an electric field. In these experiments the plasma current was driven with 0.9 MW of off-axis deposited ECCD, together with the bootstrap current. Into this target plasma, EC waves with 0.45 MW power were applied in the plasma centre. No degradation in $\tau_{Ee}$ was observed. Best performance was found with a small CNT-CD component. In this plasma, a confinement enhancement factor $H_{RLW} = 4.5$ was achieved, with the bootstrap current $I_{BS}$ being 50% of the total plasma current, and an electron internal transport barrier (eITB) sustained in steady state. The location of the barrier does not change and the pressure and current density profiles are fully non-inductively controlled. When the CNT-CD component is too large, the profiles become too steep and the plasma becomes MHD unstable. Thus, we can stay just below the MHD limit by tuning the launcher angle.

The TCV tokamak has major and minor radius $R_0 = 0.88$ m, $a = 0.25$ m, respectively. The magnetic field on axis is $B_0 = 1.4$ T. The TCV is a unique tokamak in two major

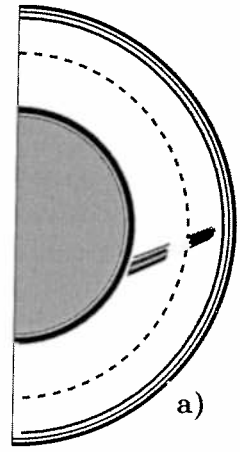


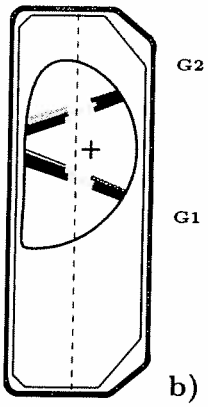


Fig. 1. a) Top and b) Side view of the plasma and the EC beams G1 and G2.

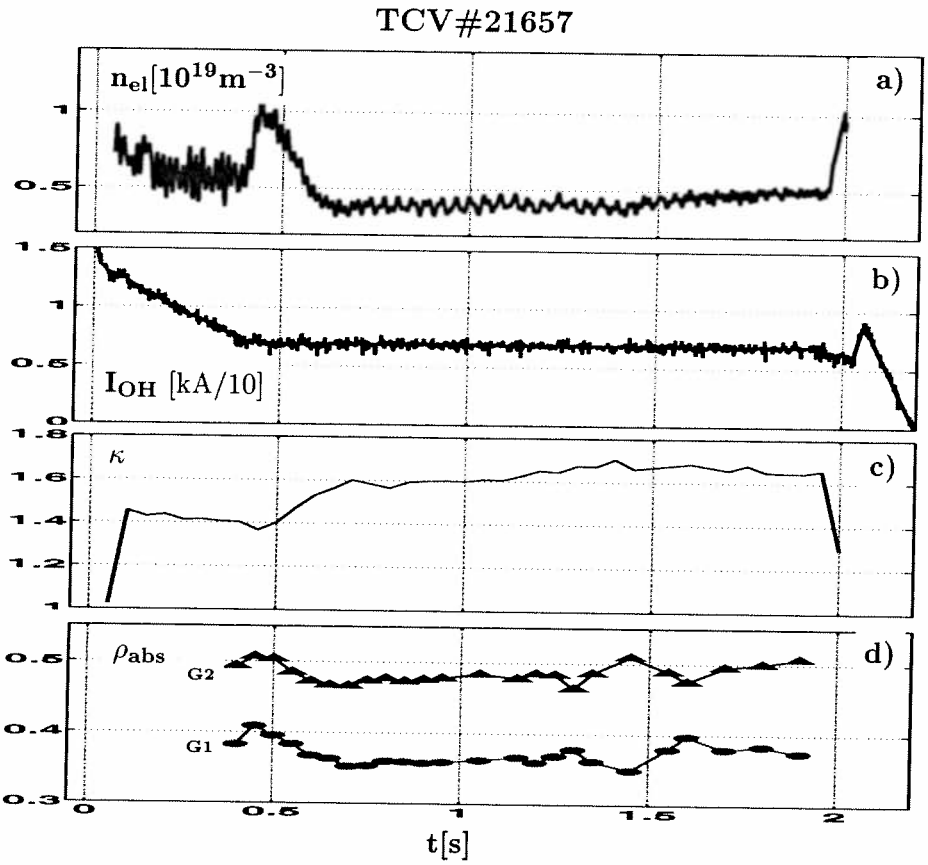


Fig 2. Time traces of a) Line averaged electron density, b) Current in the Ohmic transformer c) Elongation, and d) Power absorption location calculated with ray-tracing.

ways. First, it is possible to create plasmas with an unequaled variety of shapes, with elongation in the range 1 to 2.8 and triangularity $-0.6 \leq \delta \leq 1$. Second, the EC power density is very high, more that 10 MW/m$^3$. The electron cyclotron (EC) system of TCV consists of 6 gyrotrons with a frequency of 82.7 GHz (second harmonic X-mode, X2), a power of 0.45 MW each, and a pulse length of 2 s. These X2 gyrotrons are connected to six independent launchers which can be swept poloidally and toroidally, to heat different plasma locations with varying degrees of ECCD. Fully non-inductive discharges are routinely obtained with ECCD in TCV [5,6]. Typically, combined central and off-axis ECCD is used with an angle of $\varphi_T = 25° - 35°$ with respect to the normal to the toroidal magnetic field. In this manner we have obtained a plasma current of 200 kA, with ECCD efficiency of 0.1 A/W and densities of $1 - 2 \times 10^{19}\,\mathrm{m}^{-3}$.

The structure of the paper is as follows. In section 2a, we describe the experiment with two off-axis gyrotrons driving all the current. In section 2b, the confinement properties of this plasma are studied with central EC deposition. Modeling of the EC current density profile using a Fokker-Planck code with a radial transport model is explained in section 3. Conclusions are in section 4. The normalized radial coordinate, $\rho$, is the square root of the volume inside the flux surface.

## 2. Experiments

All the plasmas were non-inductive with the loop voltage $V_{loop} = 0$, average density in the range $n_{e,ave} = 0.5 \times 10^{19}$ m$^{-3}$, elongation $\kappa = 1.6$, and plasma current $I_p = 60 - 90$kA.

**a) Off-axis ECCD driven plasma** The basic set up was the following. First, plasma was formed with an Ohmic field. Then at 0.4s off-axis ECCD was switched on and at 0.42s the current in the Ohmic transformer was set to a constant value until the end of the discharge. Two gyrotrons, aimed off-axis with an angle of $\varphi_T = 23°$, were driving 70% of the current, the remaining 30% being supplied by the bootstrap current. See Fig. 1 for the plasma shape and the ray paths as calculated by ray-tracing. The power is absorbed in the grey region and the vertical dashed line in 1b is the cold EC resonance. The line-averaged electron density, $n_{el}$, is in Fig. 2a. The density is almost constant $n_{el} \approx 0.5 \times 10^{19}$ m$^{-3}$ during the whole ECCD phase. The current in the Ohmic transformer primary, Fig. 2b, is constant after 0.42s. As all the currents in the shaping coils are also constant after an initial transient, the Ohmic electric field vanishes. The elongation of the plasma $\kappa$ increases from 1.4 to almost 1.7, Fig. 2c, indicating a broadening of the current profile as the external shaping fields are constant. The points in Fig 2d are the radial coordinates of the mean absorption locations of the two beams. Total EC power was $P_{EC} = 0.9$ MW.

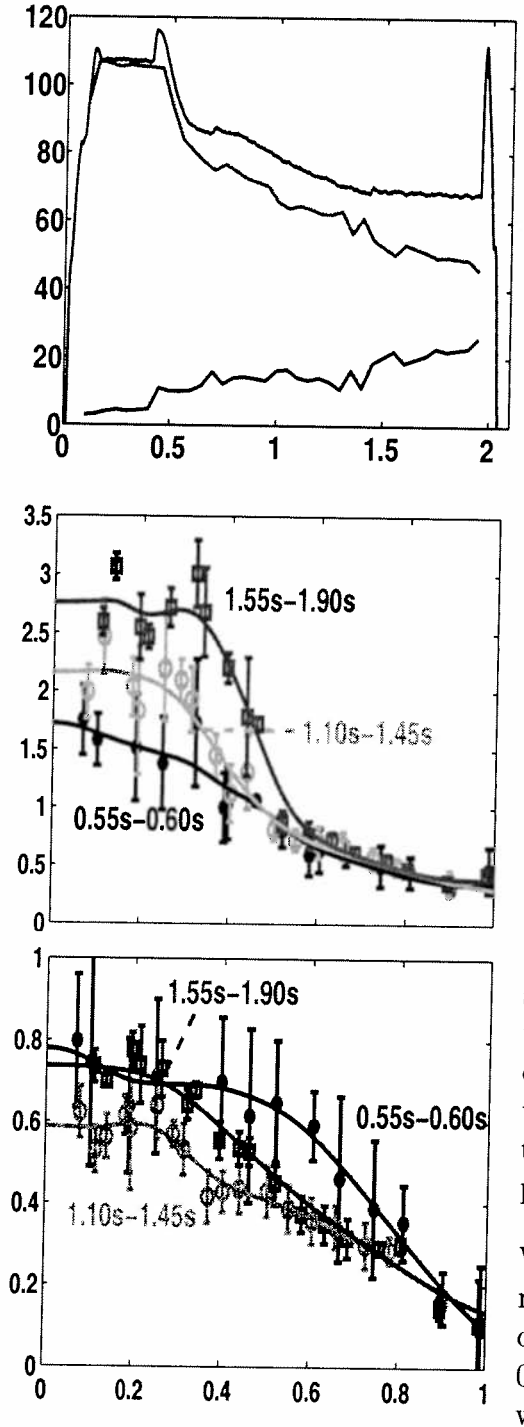


Fig. 3. a) Plasma current $I_p$, bootstrap current $I_{BS}$ calculated from Thomson profiles, and the difference $I_p - I_{BS}$. b) and c) Thomson temperature and density profiles.

The plasma current is shown in Fig. 3a. Two off-axis gyrotrons are not sufficient for sustaining a 100 kA current and $I_p$ decreases to a constant value of 70 kA at 1.4s. Also shown is the bootstrap current $I_{BS}$ calculated with Thomson electron density and temperature profiles. The asymptotic difference $I_p - I_{BS}$ is the current driven by the waves. From the Thomson profile measurements, Fig. 3b and c, we see that before 0.6s the profiles are approximately parabolic. However, at later times (>1.0 s) a steep gradient in the $T_e$ profile has been formed at the radial position $\rho \approx 0.4$, signaling the formation of a transport barrier at that location.

We note that the value of the ECCD driven current, $I_{CD} = I_P - I_{BS}$, is about 50 kA and the current drive efficiency is $\eta_{CD} = I n_{e,20}/(RP) = 0.0031$ [A,m$^{-3}$,m,W]. In usual ECCD scenario, with central ECCD, $\eta_{CD}$ is of the order of 0.01. Reduction of efficiency in off-axis ECCD is due to the lower temperature and the effect of trapped particles [5], which absorb part of the EC power but they do not carry any current.

**b) Off-axis ECCD with central EC** In this case, once the barrier had been formed, a third gyrotron with central deposition, $\rho_{abs} \leq 0.3$, was added. In Figs. 4a and b, density

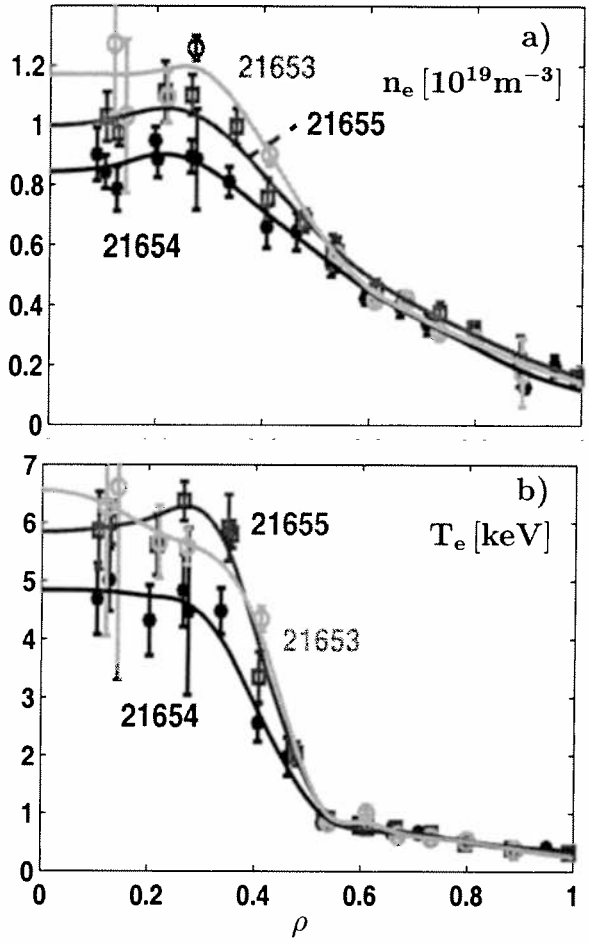


Fig. 4. Time averaged Thomson a) density and b) temperature profiles of three plasmas with off-axis ECCD and different angle of the central EC beam. A broad eITB is formed at $\rho = 0.4$.

and temperature profiles of this plasma, #21654, are shown. The profiles are time averaged over the central EC phase. The profiles are qualitatively similar to those of #21657 (only off-axis ECCD) but the gradient is steeper due to the higher energy content in the centre. In Fig. 5a we show $\tau_{Ee}$, $\tau_{RLW}$, and $H_{RLW}$. We see no degradation in $\tau_{Ee}$ even though 0.45 MW of EC power was added at 1.15s. More striking is the evolution of $H_{RLW}$, which increases from about 2 to almost 3.5. The improvement in confinement when power is deposited behind the steep gradient strongly corroborates the existence of an eITB in #21654. The barrier stays in the same location in steady state for over 1s, which is more than 500 $\tau_{Ee}$ and almost 5 $\tau_{CRT}$ ($\tau_{CRT}$ being the current redistribution time).

The question that arises is: Why do we have an eITB in off-axis ECCD driven plasmas. Because of the special current drive scheme, it is natural to hypothesize that the eITB is related to the current profile. In Fig. 5b, grey line, we show the time evolution of $T_e$ in a discharge with simultaneous start of ECCD and central ECRH at 0.4s. This plasma is similar to #21654 with an eITB at $\rho = 0.4$ and $H_{RLW} = 3.5$. The temperature rises rapidly from 1 keV to 3 keV after the onset of the EC power. After this, $T_e$ evolves much more slowly. It takes about 0.5s for $T_e$ to evolve to

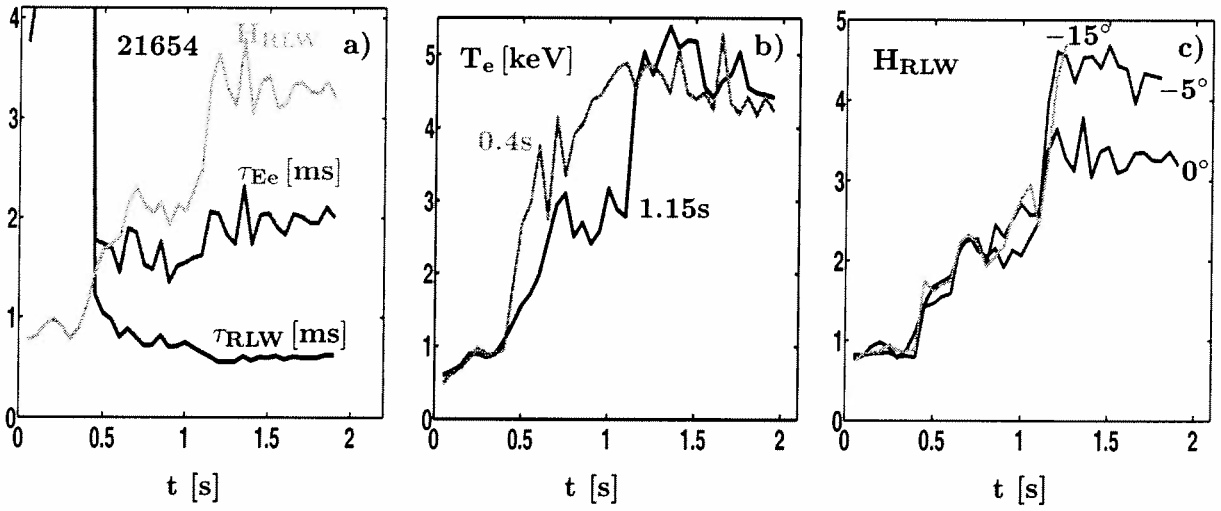


Fig. 5. a) 21654: $\tau$Ee, $\tau_{RLW}$, and $H_{RLW}$. b) Comparison of similar plasmas having different starting time of central ECRH, 0.4s and 1.15s. c) $H_{RLW}$ for plasmas with different $\varphi_T$ of the central beam. The angles are shown in the figure.

the final temperature of 4.8 keV. This slow time scale is of the order of the current redistribution time, $\tau_{CRT}$, which is approximately 200ms; by contrast, the confinement time at 0.5s is only about 1.5ms. Also shown is $T_e$ of #21654 in which ECRH was switched on at 1.15s. Before 1.15s we see that the temperature evolves slowly as the eITB is being formed, $\Delta t_2 = 0.25$s. We note that $T_1^{3/2}/T_2^{3/2} \approx \Delta t_1/\Delta t_2 \approx 2$ as expected since $\tau_{CRT} \sim T^{3/2}$. At 1.15s when the central ECRH is applied, the eITB has already been formed and $T_e$ rises on the scale of $\tau_{Ee}$. This constitutes direct proof that the formation of the eITB is related to the current profile.

In Fig. 5c we show $H_{RLW}$ for three plasmas with different $\varphi_T$ of the central beam: 21654 with 0° (ECRH), 21655 with −5°, and 21653 with −15°. The negative angle means CNT-CD with respect to the total plasma current. $H_{RLW}$ increases with increasing CNT-CD component and with the largest angle the plasma becomes MHD unstable due to overly peaked profiles. Thus, a direct control mechanism exists for staying just below the MHD limit. With a central CNT-CD angle of −5°,$H_{RLW} = 4.5$ is obtained in steady state with $T_e = 6$ keV. The eITB in all these plasmas, Figs. 4 a) and b) is clearly visible and is in the same location, $\rho = 0.4$. #21653 disrupted shortly afterwards as the profiles continued to evolve rapidly.

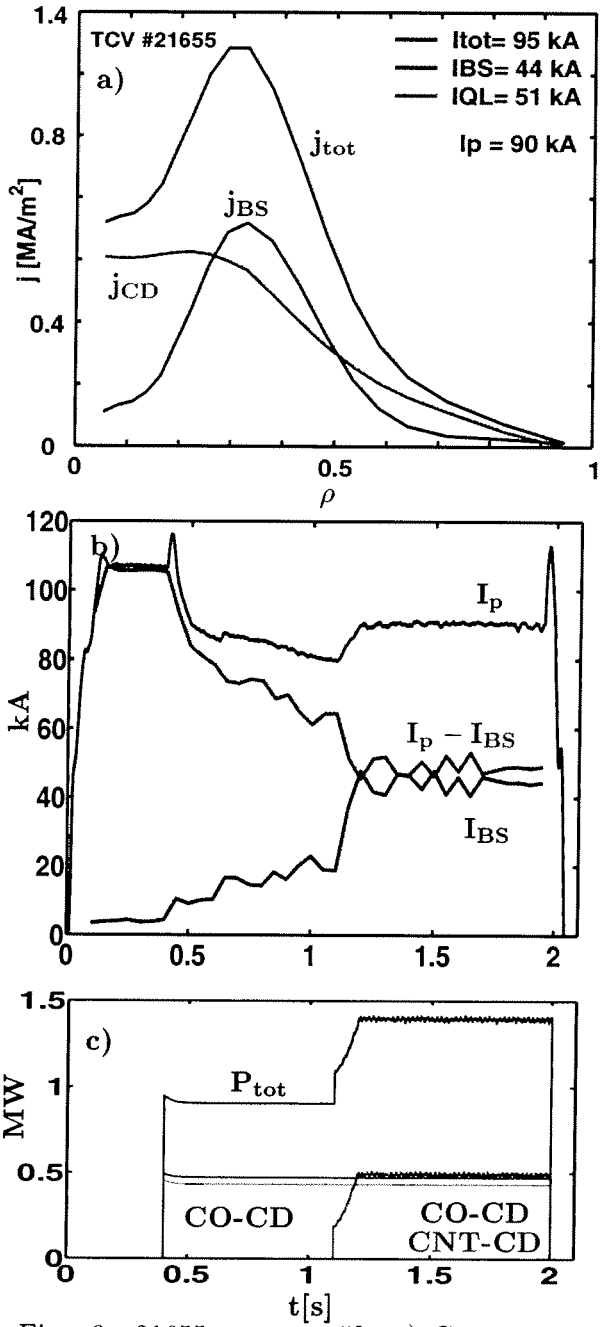


Fig. 6. 21655, $\varphi_T = -5°$: a) Current profiles, $j_{EC}$ calculated with F-P using transport model, b) plasma and bootstrap current and the difference, and c) EC beam powers.

The total current density profile, $j_{tot}$, of #21655, $\varphi_{EC} = -5°$, together with $j_{BS}$ and $j_{CD}$ are shown in Fig. 6a (modeling of $j_{CD}$ is explained in the next section). The current density profile is hollow with a maximum at $\rho \approx 0.3$. It is the bootstrap contribution which makes $j_{tot}$ hollow. From the traces of $I_p$ and $I_{BS}$, Fig. 6b, we see that $I_{BS}$ is 50% of $I_p$ due to the steep gradient in the eITB region. In Fig. 6a, $I_{tot} = I_{QL} + I_{BS}$, where $I_{QL}$ is the EC current density calculated with transport, and $I_p$ is the measured plasma current. Fig. 6c shows the EC power.

## 3. Modeling of the EC current density profile

Modeling has been performed with two codes: a linear ray-tracing code TORAY-GA [7,8] and a Fokker-Planck code CQL3D [9]. TORAY-GA solves the cold plasma dispersion relation and the ray-tracing equations to find the ray paths in the plasma. The EC wave damping calculation is based on a relativistic calculation of the imaginary part of the wave vector. The EC current is calculated in a linear approximation by assuming a small

perturbation to the background Maxwellian electron distribution function [8]. The resulting ECCD efficiency, which is independent of power, is in many cases in relatively good agreement with experiments [5,10]. These results are surprising at first sight since the formation of a suprathermal electron tail due to ECCD with power density of the order of $10\,MW/m^3$ is expected to improve the ECCD efficiency [11].

The CQL3D Fokker-Planck code solves the bounce averaged Fokker-Planck equation in two velocity and one radial dimensions. For a detailed model derivation see [12]. The equation can be written formally as

$$\frac{df(v_\perp, v_\parallel, \rho)}{dt} = C(f(v_\perp, v_\parallel, \rho)) + Q(f(v_\perp, v_\parallel, \rho)) + R(f(v_\perp, v_\parallel, \rho)) \quad (1)$$

The code uses a relativistic collision operator C(f) and a quasilinear EC wave damping term Q(f). The background is a fixed Maxwellian with momentum conserving collisions between the background and the evolving species. The ray paths from TORAY-GA are used. The real flux surface geometry is passed from the LIUQE equilibrium reconstruction [13]. The distribution function evolves due to absorption of EC waves and collisions. Also a model for radial transport R(f) can be used. The radial transport model is

$$R(f(v_\perp, v_\parallel, \rho)) = \frac{\partial}{\partial r}\left(D_r \frac{\partial}{\partial r} f + V_a f\right), \quad D_r = D_0\, g(r)\, h(v_\parallel) \quad (2)$$

where $D_r$ is the radial diffusion coefficient as defined. The magnitude of $D_r$ is given by $D_0$, the radial profile by g(r), and a dependence on the parallel velocity by $h(v_\parallel)$. These quantities must be given as input functions. Experimentally, the profile g(r) is found to be increasing with the radial coordinate in L-mode plasmas [14]. We have used a profile in the form

$$g(r) = \frac{1 + (3\rho)^3}{n_e/n_{e0}}. \quad (3)$$

Two forms for the parallel velocity dependence have been applied:

$$h(v_\parallel) = 1 \quad (4)$$

corresponds to electrostatic turbulence (E × B drift) and

$$h(v_\parallel) = \frac{v_\parallel}{(1 + L_A/\lambda_{mfp})} \quad (5)$$

represents electromagnetic turbulence [15,16]. Above, $L_A = \pi R_0 q(r)$ is the autocorrelation length of the background magnetic field, $R_0$ is the geometrical major radius, and q is the safety factor. The mean free path $\lambda_{mfp}$ is calculated from non-relativistic electron-electron and electron-ion collision rates. The advection velocity $V_a$ is adjusted by the code such as to keep the density profile unchanged.

In Fig. 7 the TORAY-GA results are compared with the CQL3D calculations for the target off-axis ECCD plasma, #21657. CQL3D was run in two ways: in the linear mode, that is with EC power scaled down by $10^{-3}$ and the results renormalized to full power, and with the true power $P_{EC} = 0.9\,MW$. The power absorption profiles are identical. TORAY-GA predicts slightly lower power absorption but the difference is not large. The current density profile is localized in the power absorption region. TORAY-GA and CQL3D predict only about half of the observed $I_{CD}$. CQL3D with true power overestimates the current by a factor of ten. The discrepancy between the linear ECCD efficiency and the experimental result mean that the quasilinear effects are important in the off-axis ECCD

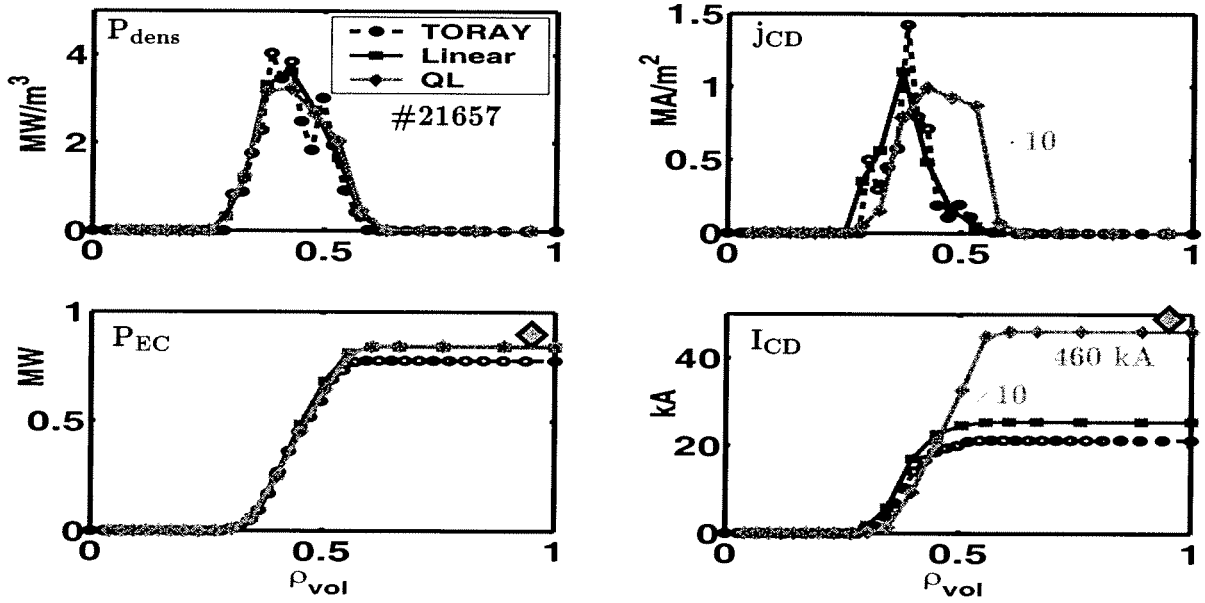


Fig. 7. TORAY, Fokker-Planck with a linear power level and F-P with quasilinear effects calculations for TCV plasma #21657, two off-axis beams. The current in the quasilinear case are scaled down by a factor of 10 for ease of plotting. TORAY and F-P in the linear regime predict half of the observed current. F-P with true power overestimates the current by a factor of 10.

plasmas. On the other hand, the quasilinear calculation leads to a large overestimation. One must then seek a mechanism that can temper the quasilinear effects. Such a mechanism is radial transport, which indeed allows the Fokker-Planck results to be in accordance with the experiment [17]. In Fig. 8 we show results with the same plasma using CQL3D with the two transport models, Eq. (4) and Eq. (5). The value $D_0$ was chosen to reproduce the observed $I_{CD} = I_p - I_{BS}$. For the electrostatic and electromagnetic cases, the values $D_0 = 5$ m$^2$/s and $D_0 = 0.4$ m$^2$/s, respectively, were required. Even though the difference in $D_0$ is an order of magnitude, the effective diffusion coefficients are similar in the velocity range of electrons which carry most of the EC current. $D_0$ is also in the range of the commonly assumed level of anomalous transport of thermal particles.

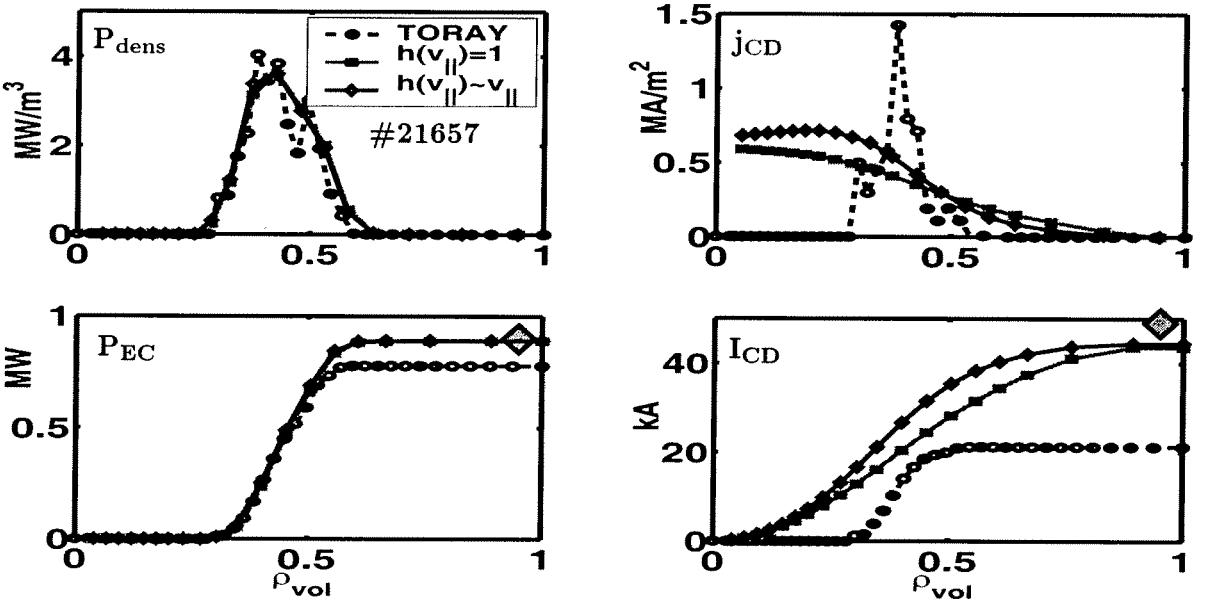


Fig. 8. TORAY and CQL3D with two different models for radial transport: radial diffusion coefficient constant in velocity space and $D_r \sim v_{||}$.

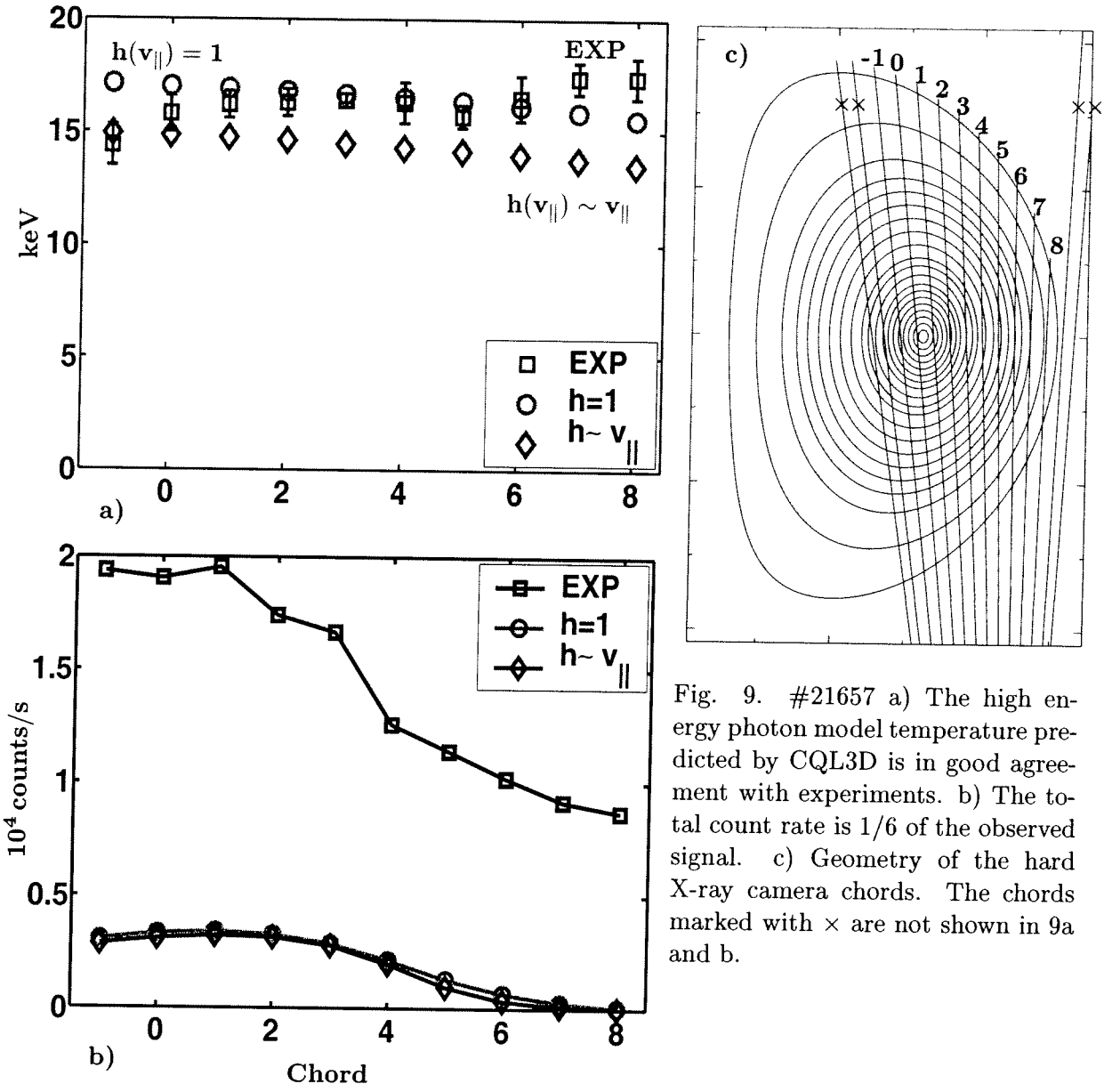


Fig. 9. #21657 a) The high energy photon model temperature predicted by CQL3D is in good agreement with experiments. b) The total count rate is 1/6 of the observed signal. c) Geometry of the hard X-ray camera chords. The chords marked with × are not shown in 9a and b.

While transport does not affect the power absorption, the current profile is very different with and without transport. The radial transport spreads the fast particles across the plasma radius leading to a smooth and flat or even centrally peaked current density profile. Note that both transport models predict similar $j_{CD}$ profiles. Based on these results, modeling of other discharges was restricted to the electrostatic case.

A comparison of the calculated Hard X-ray (HXR) signal from CQL3D with experimental measurements is shown In Fig. 9. The measurements are performed with a camera [18] on loan from CEA Cadarache. This comprises 14 viewing chords which cover the whole outer minor radius of the plasma. The radial resolution is $\sim$ 2 cm on the mid plane (see Fig. 9c). In Fig. 9a we compare the observed and calculated high energy photon temperatures determined from exponential fits to the spectra in the energy interval $40 \leq E_\gamma \leq 100$ keV. The spatial variation of the temperature is minimal, as has been observed previously [19]. The calculated temperatures are in a very good agreement and there is no significant difference between the two transport models. However, the calculated total count rates for $E_\gamma \geq 40$ keV, shown in Fig. 9b, are 1/6 of the observed values. On the other hand, in the energy range $10 \leq E_\gamma \leq 40$ keV, CQL3D overestimates the observed signal.

## 4. Summary and conclusions

Non-inductive ECCD plasmas with off-axis ECCD in TCV tokamak have been reported. The plasma current was driven by the EC waves together with a bootstrap current totaling to up to 50% of the total plasma current model($I_{BS} = 44\,kA$, $I_p = 90\,kA$). A wide steady-state eITB, located at a normalized radius $\rho = 0.4 - 0.5$, has been demonstrated by adding 0.45 MW of central EC without causing any degradation in the electron energy confinement time. A confinement enhancement factor $H_{RLW}$ up to 4.5 for more than $500\,\tau_{Ee}$ and about $5\,\tau_{CRT}$ has been achieved with a small central CNT-CD component. Both pressure and current density profiles are fully non-inductively controlled and operation close to the MHD limit is possible.

The formation of the eITB is due to a hollow current density profile and the time scale of its formation is $\tau_{CRT}$. The bootstrap current is very large due to steep gradients and it is the bootstrap current which makes the total current density profile hollow. A Fokker-Planck code with a transport model predicts the observed EC current well if a transport level of the order of the anomalous transport of thermal particles is assumed. The simulated ECCD profile is flat in the centre and nonzero up to the edge region of the plasma. The hard X-ray camera signal shows high energy electron population on the plasma boundary, in accordance with the simulated EC current profile. In addition, the code reproduces the measured hard X-ray temperature well. By contrast, linear modeling predicts only half of the observed current.

## References


[1] Z.A. Pietrzyk *et al,* Phys. Rev. Lett. **86**, (2001) 1530.

[2] R. Behn *et al,* Proc. 28th EPS Conf. on Cont. Fusion and Plasma Physics, Funchal, Madeira, 2001, Europhys. Conf. Abstr. (2001).

[3] P.H. Rebut, P.P. Lallia, M.L Watkins in Proc. 12th Int. Conf. of Plasma Physics and Controlled Fusion Research, Nice 1988, IAEA Vienna, 1989, Vol. 2, (191).

[4] A. Pochelon *et al,* , Nucl. Fusion **39** (1999) 1807.

[5] O. Sauter *et al,* Phys. Rev. Lett. **84** (2000) 3322.

[6] S. Coda *et al,* , Plasma Phys. Control. Fusion **42** (2000) B311.

[7] K. Matsuda, IEEE Trans. Plasma Sci. PS-17 (1989) 6.

[8] R.H. Cohen, Phys. Fluids **30** (1987) 2442.

[9] R.W. Harvey *et al,* Proc. of the IAEA Tech. Conf. of Advances in Simulation and Models of Thermonuclear Plasmas, IAEA, Vienna, 1992.

[10] P. Nikkola and O. Sauter, Theory of Fusion Plasmas, Int. Workshop, Varenna, Editor J.W. Connor *et al,* Editrice Compositori, Società Italiana di Fisica (2000) 345.

[11] R.W. Harvey *et al,* Phys. Rev. Lett. **62** (1989) 426.

[12] J.Killeen *et al, Computational Methods for Kinetic Models of magnetically Confined Plasmas*, Springer-Verlag 1986.

[13] F. Hoffmann and G. Tonetti, Nucl Fusion **28** (1988) 1871.

[14] K.H. Burrell *et al,* Proc. 13th Int. Conf. of Plasma Physics and Controlled Fusion Research, Washington 1990, IAEA Vienna, 1991 Plasma Phys. and Control. Nucl. Fusion Research, Vol. I (1991) 123.

[15] A.B. Rochester and M.N Rosenbluth, Phys. Rev. Lett. **40** (1978) 38.

[16] R.W. Harvey *et al,* Phys. Rev. Lett **47** (1981) 102.

[17] R.W. Harvey *et al,* Phys. Rev. Lett. **88** (2002) 205001.

[18] S. Coda *et al,* Proc. 26th EPS Conf. on Cont. Fusion and Plasma Physics, Maastricht 1999, Europhys. Conf. Abstr. **23J** (1999) 1097.

[19] S. Coda *et al,* Proc. 28th EPS Conf. on Cont. Fusion and Plasma Physics, Madeira 2001, Europhys. Conf. Abstr. **25A** (2001) 301.

# RADIAL TRANSPORT EFFECTS ON ECCD IN THE TCV AND DIII–D TOKAMAKS AND ON OHMIC DISCHARGES IN THE MST RFP

R.W. Harvey,[1] O. Sauter,[2] R. Prater,[3] P. Nikkola,[2] R. O'Connell,[4] and C.B. Forest[4]

[1]*CompX, P.O. Box 2672, Del Mar, California 92014-5672*
[2]*Ecole Polytechniuque Fédérale de Lausanne, CH-1015, Lausanne, Switzerland*
[3]*General Atomics, P.O. Box 85608, San Diego, California 92186-5608*
[4]*University of Wisconsin, Madison, Wisconsin 53706-1687*

The comprehensive CQL3D Fokker-Planck/Quasilinear simulation code has been benchmarked against experiment over a wide range of electron cyclotron conditions in the DIII–D tokamak (C.C. Petty et al., 14th Topical Conf. on RF Power in Plasmas, 2002). The same code, in disagreement with experiment, gives 560 kA of ECCD for a well documented, *completely ECCD-driven*, 100 kA TCV shot [O. Sauter et al, PRL, 2000]. Recent work (R.W. Harvey et al, Phys. Rev. Lett., 2002) has resolved the differences as due to radial transport at a level *closely consistent* with ITER scaling. Transport does not substantially affect DIII–D ECCD, but at similar ECH power has an overwhelming effect on the much smaller TCV. The transport is consistent with electrostatic-type diffusion ($D_{\rho\rho}$ constant in velocity-space) and not with a magnetic-type diffusion ($D_{\rho\rho} \propto |v_{\|}|$).

Fokker-Planck simulation of Ohmic reversed field pinch (RFP) discharges in the MST device reveals transport velocity dependence stronger than $|v_{\|}|$ will give agreement with current and soft X-ray spectra in standard discharges, but in the higher confinement, current profile controlled PPCD discharges, transport is again electrostatic-like. This is consistent with the object of PPCD, which is to replace magnetic turbulence driven current with auxiliary CD to improve transport. The tokamak and high-confinement RFP results mutually reinforce the constant-in-velocity-space "electrostatic-type turbulence" conclusion. The steady-state energy and toroidal current are governed by the same radial transport equation.

The role of radial transport on high energy electrons in tokamaks and reversed field pinches (RFPs), particularly in regards to radiofrequency (rf) experiments, has been examined by several authors [1–8, and references therein]. At high enough power, the plasma temperature is high and the transport effects strong enough such that radial transport dominates the collisional slowing down time of the fast electrons. Our calculations [8] show that this is strongly the case for a representative full-toroidal-current-drive electron cyclotron current drive (ECCD) experiment [9] in the TCV fusion energy tokamak. Although there is little doubt as to whether plasma turbulence is responsible for the observed radial transport in excess of collisional levels [10], questions remain on the extent electrostatic (ES) or magnetic turbulence dominates [11] and also the degree of concurrence between tail electron transport and bulk plasma transport. In tokamaks our work shows good agreement between experiment and modeling based on radial diffusion due to ES turbulence at a level predicted by well-known empirical modeling [10]; it shows poor agreement with the purely magnetic turbulence model.

In the MST reversed field pinch (RFP) device at UW, Madison, a similar result has been found: In standard Ohmic MST discharges the transport appears to be due to magnetic-type turbulence; however, when the plasma current driven by magnetic turbulence in the outer part of the plasma is replaced by transiently driven Ohmic pulsed poloidal current (PPCD), the transport improves and switches from magnetic-type to being dominated by electrostatic-type [12].

The primary results for DIII–D and TCV have been reported in Ref. 8. In this paper we report on further aspects of the calculation, and outline some of the new, related results being obtained in the MST device.

The calculations are performed with the comprehensive CQL3D Fokker-Planck/Quasilinear (FP/QL) simulation code [4]. The FP model includes two-dimensional in momentum-space collisional diffusion, the full Stix [13] rf QL diffusion coefficient, a radial diffusion $D_{\rho\rho}$ and pinch term in non-circular flux-surface geometry, and is relativistic. The pinch term is adjusted to maintain a target density profile. Steady-state, finite-difference numerical solutions are obtained for the electron distribution $f_e(u_0,\theta_0,\rho)$, evaluated at the outer equatorial plane of the toroidal plasma, where $u_0 = p/m_e$ is momentum-per-electron-rest-

mass, $\theta_0$ is momentum-space pitch angle, and $\rho$ is a generalized radial coordinate labeling the toroidal flux surfaces. For the TCV modeling, the velocity dependence of $D_{\rho\rho}$ is chosen to be either constant (ES turbulence-type) or proportional to the magnitude of the electron velocity $|v_{\|}|/v_{T_e}$ parallel to the ambient magnetic field (magnetic turbulence type) divided by the thermal velocity $v_{T_e} = (T_e(\rho)/m_e)^{1/2}$. The radial dependence of $D_{\rho\rho}$ is chosen to increase towards the plasma periphery, $D_{\rho\rho} = D_{\rho\rho 0}(1+3(\rho/a)^3)(n_{e0}/n_e(\rho))$ in general accord with experimental observations for the relevant low confinement L–mode [14]. The EC radiation field is obtained from data coupled into CQL3D from the TORAY-GA [15] ray tracing code. We expect that, using the experimentally measured profiles of plasma density ($n_e$), temperature ($T_e$), and effective charge $Z_{eff}$, the CQL3D facility can provide a full and accurate physics-based model of the ECCD process in tokamaks, apart from the radial transport effects which are to be discerned by comparison with experiment.

The CQL3D code is run with collisions of the electron distribution occurring on ions and on a self-consistent distribution of the electrons for which the angular dependence is expanded in Legendre polynomials, except that the coefficient of the $P_0(\theta_0)$ term is maintained at the Maxwellian corresponding to the radially local experimental temperature. This has the effect of maintaining the local bulk of the electron distribution as a Maxwellian with the experimental parameters; the tail electrons then collisionally interact with the dominant bulk and radially diffuse. Momentum is conserved in the electron-electron interaction, preserving accurate determination of the parallel current.

To perform an accurate comparison between radial diffusion of the tail particles and a given (ITER) confinement scaling [10], it is necessary to account for the 2-D, non-circular effects. These are treated in a manner consistent with the ONETWO transport code [16].

We consider the radial transport of the quantity $\lambda f / \oint (dl_B/\psi)$ which is the flux surface volume-average of particles in the momentum-space element $d^3\mathbf{u}_0$. Quantity $\psi = B/B_0$, and $l_B$ is length along $\mathbf{B}$; B is magnetic field strength and $B_0$ its minimum value on a flux surface. The radial operator conserves flux surface averaged density $\langle n \rangle = \int d^3\mathbf{u}_0 \lambda f / \oint (dl_B/\psi)$. For noncircular geometry, we obtain[4]

$$\frac{\partial(\lambda f)}{\partial t} = \langle\langle R \rangle\rangle + \ldots = \left|\frac{\mathbf{u}_{\|0}}{B_0}\right|^{C_0} \frac{\oint dl_B/\psi}{H\rho} \left.\frac{\partial}{\partial\rho}\right|_{C1,C2} H\rho \left|\frac{B_0}{\mathbf{u}_{\|0}}\right|^{C_0} \cdot \left\{ D_{\rho\rho} \left.\frac{\partial}{\partial\rho}\right|_{C1,C2} \left[ \frac{\lambda f}{\oint (dl_B/\psi)} V_p \frac{\lambda f}{\oint (dl_B/\psi)} \right] \right\} \tag{1}$$

where

$$(C_0, C_1, C_2) = \begin{cases} (1,\ E,\ u) & \text{constant E, u diffusion} \\ (0,\ \mu_0,\ \theta_0) & \text{constant } u_0, \theta_0 \text{ diffusion} \end{cases} .$$

H is a quantity previously used in the ONETWO transport code [16] containing the effects of noncircular geometry, and is equal to 1, for circular concentric flux surfaces. The quantity $u_{\|0}/B_0$ appears in the Jacobian of the transformation from $u_0,\theta_0$- to E,$\mu$-coordinates, $d^3\mathbf{u}_0 = |B_0/\mathbf{u}_{\|0}|(2\pi\gamma/m^2)dEdu$ The radial diffusion coefficient $D_{\rho\rho}$ and the advective pinch term $V_\rho$ are arbitrary functions of velocity and radius. The above radial transport equation is in a conservative form. In the present work, we have used "constant $u_0,\theta_0$-diffusion," although "constant E,$\mu$-diffusion is appropriate for turbulence below the cyclotron frequency. Taking momentum-space moments of the above radial transport operator gives the radial transport terms in the ONETWO code.

The agreement between DIII–D tokamak EC experiments and the CQL3D code has been excellent over a wide range of EC experiments and injection conditions [17], neglecting radial transport effects. The experiments discussed here on TCV and DIII–D are very similar: plasma densities and temperatures and magnetic field strength are almost the same; approximately 1.5 MW of X–mode EC radiation is injected from the off-midplane outboard side of the tokamak to resonate with plasma electrons near the second harmonic of the cyclotron frequency. The major difference between the two tokamaks is that DIII–D is 2.5

times greater in each linear dimension, or approximately 15 times the volume of TCV. Hence EC power density in the TCV tokamak is overwhelmingly stronger than in DIII–D.

A key point in regard to the TCV and DIII–D tokamaks is that they both provide data for the ITER empirical transport studies [10] and are consistent with the same transport scaling laws as fit the data from the other nine tokamaks in the data base. Thus, we may expect that transport in these devices is governed by the same general turbulence processes.

We examine the TCV shot 16099 which is fully supported by EC current drive [9]. The EC ray geometry is shown superimposed on a cross-section of the toroidal flux surfaces in Fig. 1. Spreading the 1.5 MW of EC heating and CD as shown in the figure results in a stable discharge for the 2.0 s duration of the available EC power [9].

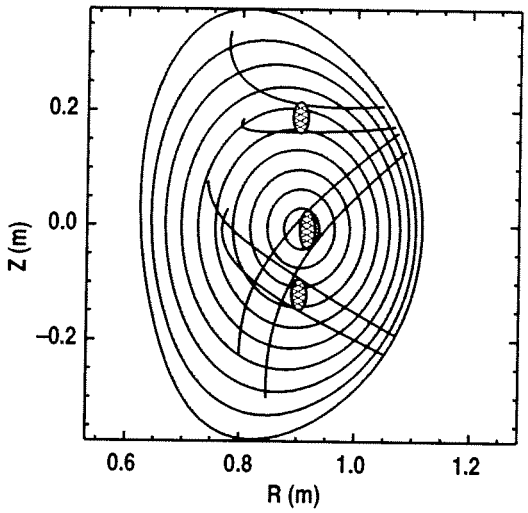


*Fig. 1. Cross-section of toroidal plasma showing ray cones and heating regions for TCV shot 16099.*

In the absence of radial transport, the calculated ECCD in TCV is 550 kA, more than 5 times the experimentally measured value. The effect of radial transport in reduction of current drive efficiency in the very high power EC experiment in TCV is dramatic. ITER L–mode scaling [10] applied to TCV shot 16099 gives confinement time 2.5 ms, as compared to the experimentally determined value 2.1 ms [9]. Transforming this to an estimate of the radial diffusion coefficient $D_{\rho\rho 0} = 0.5 * a^2/4\tau_{E,th}^L$ (the "0.5" accounts approximately for the radial dependence of $D_{\rho\rho}$ gives $D_{\rho\rho 0} = 3.0$ m$^2$ s. The value of $D_{\rho\rho 0}$ necessary in order to fit the observed EC driven current obtained for the electrostatic-type diffusion is $D_{\rho\rho 0} \approx 3.7$ m$^2$ s, whereas for the magnetic-type diffusion the value is 0.35 m$^2$/s.

If the magnetic turbulence were increased sufficiently to fit the bulk electrons, it would be a factor of 10 too strong for the code to match the observed ECCD. Thus, the results reported here provide strong support for ES-type turbulence, not purely magnetic turbulence, dominating both the bulk and the tail electron transport. On the other hand, there is the possibility that a more complicated velocity dependence of $D_{\rho\rho}$ will give the same good fit to the data as has been reported here. This will be the subject of further studies.

We now provide further detail on the simulation of TCV. At the top of Fig. 2 are shown cuts at constant pitch angle through the electron distribution for plasma radius 0.1a, and below them are the corresponding specific current density $j_u(u)$ versus $u/v_{T_e}$, where current density $j = \int j_u(u)du$. The case (a) at the left of the figure is with no radial diffusion, and the case (b) at the right is with ES-type radial diffusion coefficient 3.7 m$^2$/s. The lower-u portion of the distribution remains Maxwellian at the given experimental temperature. Without radial diffusion a large current carrying tail distribution is formed out to near the edge of the velocity-mesh.

The average electron energy versus radius is shown in Fig. 3. In the absence of transport, huge average energy is carried by the nonthermal tail. With transport, values

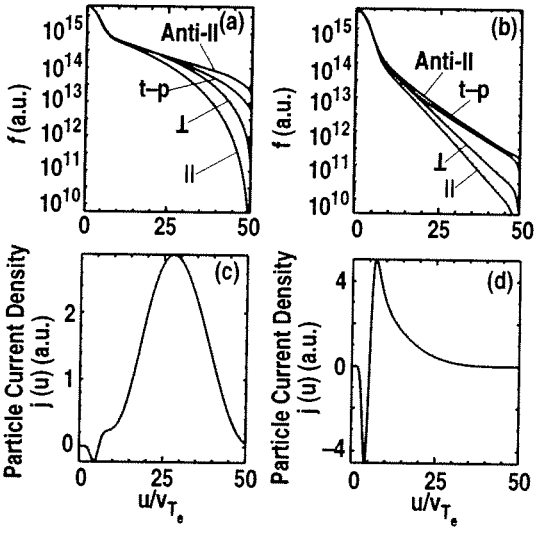


*Fig. 2. Left column (a) shows cuts through the distribution as a function of u, at various pitch angles; below is the distribution $j_u(u)$ of driven current, resulting from ECCD in TCV with no radial diffusion. The right column (b) is the same, but calculated with radial diffusion turned on.*

compatible with the experiment are obtained. In the figures, $D_{rr0}$ is the same as $D_{\rho\rho 0}$.

Transport sharply reduces the tail electron current to the 100 kA experimental value, as shown in Fig. 4. This current is slightly above the 82 kA obtained linearly in CQL3D by evaluating CD at a very low power in the absence of $D_{\rho\rho}$ and renormalizing back to the experimental power. The CQL3D linear value is slightly greater than the 70 kA from the TORAY code, based on the Cohen [18] model (which neglects current excited in the thermal portion of the electron distribution by the electron-electron collisions). The central value of current density $j(\rho = 0)$ has been reduced to a value giving safety factor $q$ =1.0, in agreement with the marginal MHD stability of this shot [9].

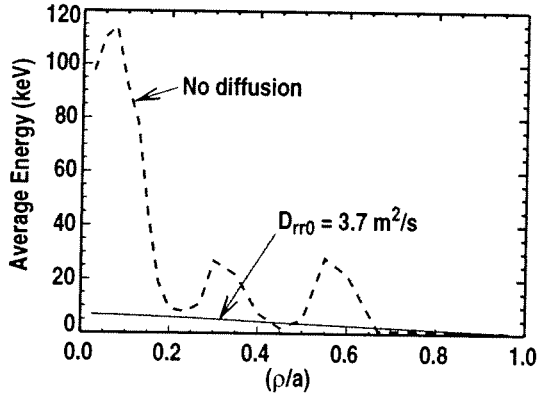


*Fig. 3. Average plasma energy in TCV, calculated without and with radial diffusion.*

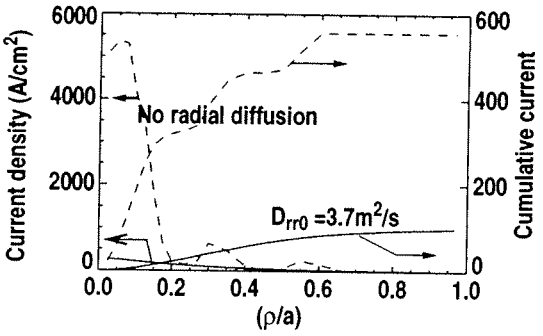


*Fig. 4. Radial profile of current density in TCV, calculated without and with radial diffusion.*

The DIII–D data [17] was modeled under the condition that radial transport is turned off in the code. In fact, a scan of ES $D_{\rho\rho 0}$ from 0 to 4.0 $m^2/s$ gives the result that the rf driven current (including synergy with the induced toroidal electric field) only reduces from 45.1 kA to 40.0 kA, for a standard benchmark shot (#104017). This change in current is within the experimental error bars. The value $D_{\rho\rho 0}$ = 1.0 $m^2/s$ is obtained from the ITER L–mode $\tau^L_{E,th}$-scaling for this shot, as previously discussed. The resulting calculated radial current density profiles are shown in Fig. 5. Thus, although the DIII–D analysis for CD efficiency which is the focus of comparison with CQL3D thus far, is not appreciably changed, there is an important spreading of the driven EC current. This effect may need to be considered for accurate calculation of EC stabilization of neo-classical tearing modes [9–22].

The standard RFP relies on transport and dynamo effects of overlapping islands associated with neoclassical tearing modes to flatten its current profile, maintaining a stable $q<1$ equilibria. Numerical studies suggested that these modes could be stabilized by flattening the current profile by driving current in the edge, thus improving confinement. This has been done on the Madison symmetric torus (MST) by the application of PPCD. The mode amplitudes fall dramatically and there is a corresponding order of magnitude increase in the confinement time to 10 ms and hard X-rays (HXRs) are seen for the first time in an RFP.

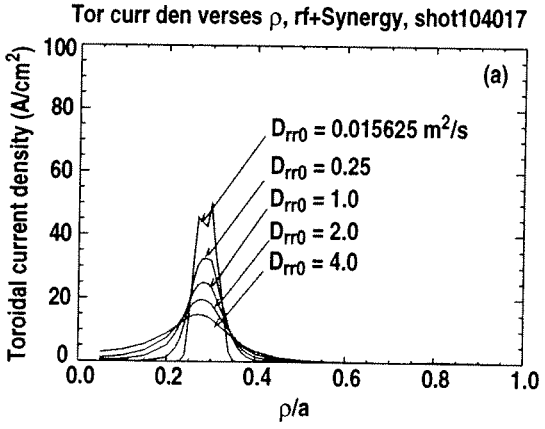


*Fig. 5. Calculated radial profile of current density in the DIII–D experiment, shot 105017, for various levels of radial diffusion. $D_{rr0}$=1.0 $m^2/s$ matches the ITER L–mode scaling.*

Given the basic plasma profiles, CQL3D has been used to model the PPCD period of these plasmas. Density, temperature, and $Z_{eff}$ (in the PPCD discharges) are measured. $E_\phi$ and $j_{||}$ are determined from the time-dependent equilibrium reconstructions. In the FP code, the applied electric field is iterated until the driven current matches the measured equilibrium current. The diffusion coefficient is left as a free variable as a function of space and energy. Best agreement with predicted CQL3D X-ray flux is for a diffusion

coefficient of ~ 1 $m^2/s$ *independent of velocity* (see Fig. 6). The plasma resistivity, which is a good indicator of the bulk electron behavior is also best fit by a diffusion coefficient of ~ 1 $m^2/s$, as shown in Fig. 7. This suggests that the transport is no longer dominated by stochastic magnetic diffusion, rather electrostatic diffusion.

In conclusion, we have shown that, for the TCV and DIII–D EC tokamak experiments which span a substantial range of the ITER transport scaling data base, the calculation of the radial transport effects at levels predicted by the ITER data base maintains agreement between experimental observations of ECCD and accepted ECCD physics. In TCV, the transport effect is overwhelming, and the agreement with transport scaling laws is accurate. Electrostatic-type turbulence is implied, and not purely magnetic-type turbulence. In DIII–D, as the EC system power is increased transport will also become more prominent. The X-ray signals indicate that, in the improved PPCD regime of the RFP, the MST device is also achieving a regime of transport dominated by electrostatic turbulence.

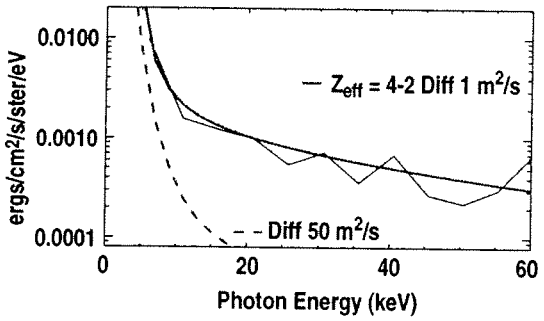


*Fig. 6. HXR flux which is indicative of fast electron behavior is best matched by a diffusion coefficient of ~ 1 $m^2/s$.*

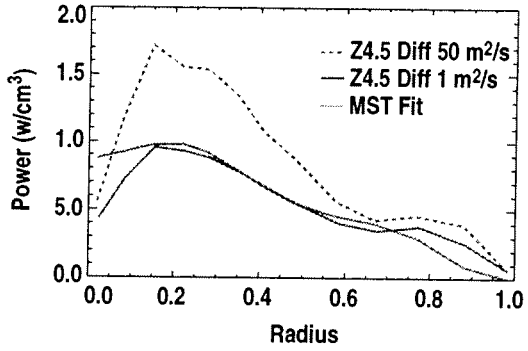


*Fig. 7. Ohmic power deposition profile which is mostly indicative of bulk electron behavior is also best modeled by a diffusion coefficient of ~ 1 $m^2/s$.*

## Acknowledgment

Work supported by U.S. Department of Energy under Contract DE-AC03-99ER54463 and Grant DE-FG03-99ER54541.

## References

[1] M.G. McCoy and R.W. Harvey, "Effects of Anomalous Transport on LH Electron Heating," Proc. 4th Topical Conf. on RF Plasma Heating, C7, R.D. Bengtson and M.E. Oakes Eds., UT, Austin (1981).
[2] B. Lloyd *et al.*, Nucl. Fusion **28**, 1013 (1988).
[3] R.W. Harvey, M.G. McCoy, and G.D. Kerbel, Phys. Rev. Lett. **62**, 426 (1989).
[4] R.W. Harvey and M.G. McCoy, Proc. of IAEA TCM on Numerical Modeling of Plasmas, Montreal, pp. 489-526, 1992 (IAEA, Vienna, 1993).
[5] Y. Peysson, Plasma Phys. Control. Fusion **35**, B253 (1993).
[6] G. Giruzzi and E. Martines, Phys. Plasmas **1**, 2653 (1994); G. Giruzzi *et al.*, Phys. Rev. Lett. **74**, 550 (1995).
[7] A.G. Peters and E. Westerhof, Phys. Plasmas **3**, 1628 (1996).
[8] R.W. Harvey, O. Sauter, R. Prater, and P. Nikkola, to be published in Phys. Rev. Lett. 88, No. 20 (2002); see also, P. Nikkola, O. Sauter, *et al.*, this conference.
[9] O. Sauter, *et al.*, Phys. Rev. Lett. **84**, 3322 (2000).
[10] *ITER Physics Basis, Chapter 2: Plasma confinement and transport*, Nucl. Fusion **39**, 2175 *ff* (1999).
[11] J.W. Connor, Plasma Phys. Control. Fusion **35**, B293 (1993).
[12] R. O'Connell *et al.*, APS2001.
[13] T. H. Stix, Waves in Plasmas, AIP, N.Y. (1992).
[14] K.H. Burrell *et al.*, in Plasma Phys. and Control. Nucl. Fusion Research, (Proc. 13th Int. Conf., Washington, 1990), Vol. 1, 123 (1991); also, our Ref. [7]; M.R. Wade *et al.*, Phys. Plasmas **2**, 2357 (1995).

[15] K. Matsuda, IEEE Trans. Plasma Sci. **17**, 6 (1989); A.H. Kritz *et al.*, Proc. 3rd Joint Varenna-Grenoble International Sym. on Heating in Toroidal Plasmas, Brussels (Oxford NY, 1982), **2**, 707.
[16] W.W. Pfeiffer, R.H. Davidson, R.W. Miller, and R.E. Waltz, "ONETWO: A Computer Code for Modeling Plasma Transport in Tokamaks:, General Atomics Report GA-A16178 (1980); F.L. Hinton and R.D. Hazeltine, Rev. Mod. Phys. **48**, 239 (1976).
[17] C.C. Petty et al., to be published in AIP Proc. of the 14th Topical Conf. on RF Power in Plasmas, Oxnard, 2001; T.C. Luce *et al.*, Phys. Rev. Lett. **83**, 4550 (1999); C.C.Petty, et al., Nucl. Fusion, **35**, 773 (1995).
[18] R.H. Cohen, Phys. Fluids **30**, 2442 (1987); **31**, 421 (1988).
[19] O. Sauter et al., Phys. of Plasmas **4**, 1654 (1997).
[20] H. Zohm, Phys. Plasmas **4**, 3433 (1997).
[21] R.W. Harvey and F.W. Perkins, Nucl. Fusion **41**, 1847 (2001).
[22] R. Prater et al., this conference (2002).

# Current profile tailoring with far off-axis ECH power deposition in TCV elongation experiments

**Y. Camenen, A. Pochelon, F. Hofmann, C. Angioni, T.P. Goodman, M.A. Henderson, P. Nikkola, L. Porte, O. Sauter**

Centre de Recherche en Physique des Plasmas, Association EURATOM-Confédération Suisse, Ecole Polytechnique Fédérale de Lausanne, 1015 Lausanne, Switzerland

## 1. Introduction

Shaping is a means to improve tokamak plasma performance. In order to test the β-limit predicted by ideal MHD for highly elongated plasmas, one has to achieve discharges at a plasma current $I_N$~2 MA/mT. Highly elongated discharges are, however, vertically unstable (axisymetric mode) and can only be stabilized by providing sufficient current density close to the plasma edge. For ohmic discharges, this implies using a low safety factor $q_{edge}$, thus a high plasma current $I_p$. In TCV, ohmic plasmas with an elongation between 2.2 and 2.8 are stabilized at a high normalized current $I_N=I_p/aB$~2.8-3.5 MA/mT [1]. Ohmic discharges are no longer stable at lower $I_N$.
To extend the range of equilibria to lower $I_N$, current profile broadening by a non-ohmic method is required. Far off-axis 2nd harmonic X-mode ECH has been tested in TCV and has allowed the creation of highly elongated discharges (κ~2.4) at low current and high safety factor ($I_N$~0.84 MA/mT, $q_{edge}$~12) [2]. At higher current, more ECH power is needed to broaden the current profile and it becomes important to develop efficient current profile broadening methods. In order to exhibit the parametric dependences of far off-axis ECH current profile broadening a series of scans have been completed. Results are presented in this paper.

## 2. Description of the experiments

The TCV 2nd harmonic electron cyclotron wave system is composed of 6 gyrotrons at 82.7 GHz, with 500 kW power per gyrotron (total 3 MW). The power is coupled to the plasma by 6 independent low field side launchers (4 upper lateral and 2 equatorial) with steering mirrors for controlling the power deposition radius during the discharge in real time.
In the experiments presented in this paper, the ohmic target plasma has an intermediate elongation (κ~1.75) and a low triangularity (δ~0.3) to avoid indentation during the EC heating phase. Between t=0.55 s and t=1.75 s, the 2nd harmonic X-mode is excited in the plasma. The EC power is deposited far off-axis ($\rho_{dep} = \sqrt{V/V_{max}} > 0.5$). Upper lateral launchers are preferred to equatorial launchers because the beam path in the plasma is shorter and is nearly normal to the flux surfaces. This makes the upper lateral launchers far less sensitive to refraction effects and thus the power deposition radius is easier controlled at high density or during a density excursion. The discharge is pre-programmed with constant quadrupole and hexapole field throughout the ohmic and the EC heated phase. The plasma current is kept constant by feedback control. The local EC deposition leads to a local increase of the temperature which modifies the resistivity profile. The inductive current profile is consequently broadened and the constant quadrupole field implies an increase of the plasma elongation κ. The feedback on the plasma current causes a drop in the loop voltage (Figure 1).
The standard operation parameters are :

$I_p$~300kA, low current to have a strong current profile modification by EC heating,
$n_{eo}$~2.5 $10^{19}$ $m^{-3}$, low density to avoid X2 cut-off or strong refraction,
$P_{EC}$~1 MW, half of the upper lateral launchers available power tohave the possibility to increase or decrease the injected power,
$\rho_{dep}$~0.7 at the beginning of the EC heating phase because this is the theoretical optimum for current profile broadening,
Fixed launchers with the same $\rho_{dep}$ ($\Delta\rho$=0), no toroidal angle (φ=0), for the ease of pre-programing and analysis and because the κ(t) evolution is unknown, a priori.

Then, various fields are explored to find the optimal current profile broadening configuration :
$0<P_{EC}<1.8$ MW : power scan,
$-20^{o}<\varphi<20^{o}$ : EC waves toroidal injection angle scan,
$0<\Delta\rho_{dep}<0.2$ : EC power deposition offset scan.
$270<I_p<420$ kA : current scan,
$0.1<\rho_{dep}<0.8$ : normalized deposition radius scan.

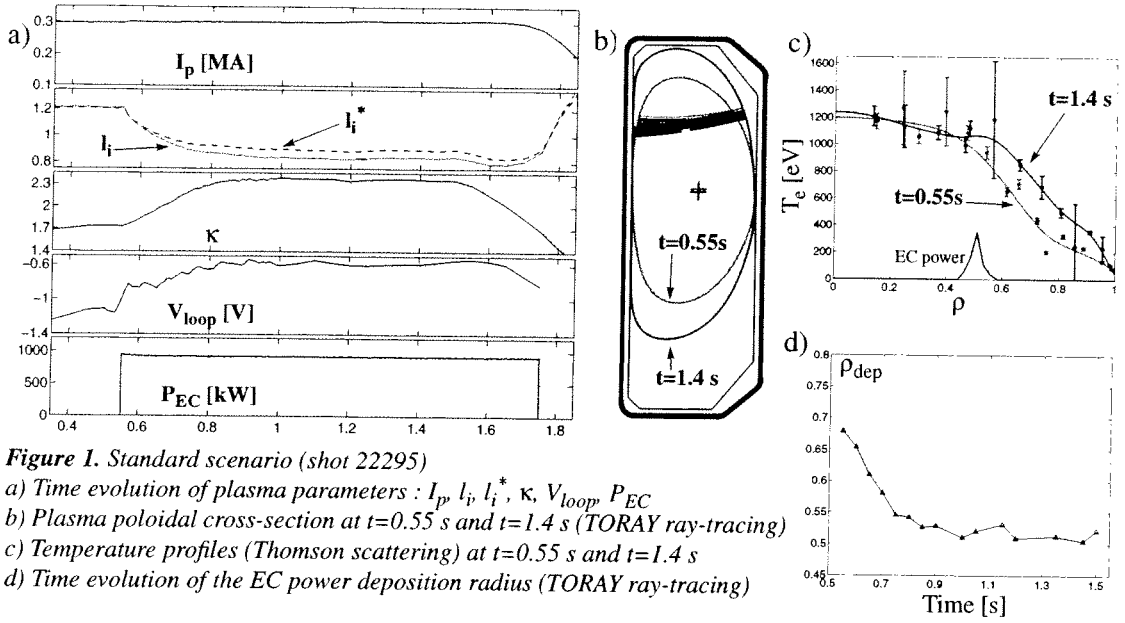


***Figure 1.*** *Standard scenario (shot 22295)*
*a) Time evolution of plasma parameters : $I_p$, $l_i$, $l_i^*$, κ, $V_{loop}$, $P_{EC}$*
*b) Plasma poloidal cross-section at t=0.55 s and t=1.4 s (TORAY ray-tracing)*
*c) Temperature profiles (Thomson scattering) at t=0.55 s and t=1.4 s*
*d) Time evolution of the EC power deposition radius (TORAY ray-tracing)*

## 3. Tools for analysis

### 3.1 Current profile indicators

*3.1.1 Plasma elongation*

Since the quadrupole and hexapole fields are kept constant during the discharge, a plasma elongation increase is necessarily due to a broadening of the current profile and a plasma elongation decrease to a current profile peaking.

*3.1.2 Temperature profile*

The modification of the current profile is essentially due to the modification of the resistivity profile (ECCD and bootstrap current represent ~8% of the total plasma current), so that the temperature profile is also an indicator of the current profile in the asymptotic limit.

*3.1.3 Internal inductance*

The internal inductance $l_i$ is computed by the equilibrium reconstruction code LIUQE using magnetic measurements [3] :

$$l_i = \frac{4}{\mu_0 I_p^2 R_0}\int\frac{B_{pol}^2}{2\mu_0}dV$$

Where $B_{pol}$ is the poloidal magnetic field and $R_0$ is the major radius.
Let us assume that all the flux surfaces have the same shape and that the toroidal current is constant on a flux surface. In a cylindrical model, $l_i$ can then be written as :

$$l_i = \frac{4\pi S^3}{I_p^2 l^2}\int_0^1\left[\int_0^\rho \tilde{\rho}\, j(\tilde{\rho})d\tilde{\rho}\right]^2\frac{d\rho}{\rho}$$

S is the plasma cross section area, l is a parameter depending on the plasma cross section perimeter and on the poloidal magnetic field, $I_p$ is the toroidal plasma current and j(ρ) is the current profile.
The internal inductance decreases when the elongation increases or when the current profile is broadened. If κ increases from 1.75 to 2.4, without any change of the current profile, $l_i$ decreases by 8%. To separate the direct plasma shape influence, we can define :

$$l_i^* \propto l_i \cdot \frac{l^2}{4\pi S}$$

The proportionality constant has been chosen to have $l_i^* = l_i$ at the beginning of the EC heating, for the standard shot. We define $\Delta l_i^*$ as the difference between $l_i^*$ at the beginning of the EC phase and $l_i^*$ during the plateau period and use it as an indicator of the current profile broadening.

### 3.2 TORAY-GA and PRETOR

The ECH deposition location and the first-pass power absorbed by the plasma are computed with the ray tracing code TORAY-GA [4].
The experimental results were compared to the fixed boundary transport code PRETOR based on the RLW model [5]. The values of the internal inductance computed by LIUQE and the ones computed by PRETOR are slightly different. In ohmic plasmas, $l_{i\,LIUQE}$ is higher than $l_{i\,PRETOR}$ by about 6%, whereas in the ECH phase $l_{i\,PRETOR}$ is higher than $l_{i\,LIUQE}$ by around 10%. The difference can be due to the fact that LIUQE prescribes quadratic current profiles for the equilibrium reconstruction while with far off-axis ECH current profiles clearly deviate from the quadratic assumption as suggested by the temperature profile of figure 1c.

## 4. Results

### 4.1 Power scan

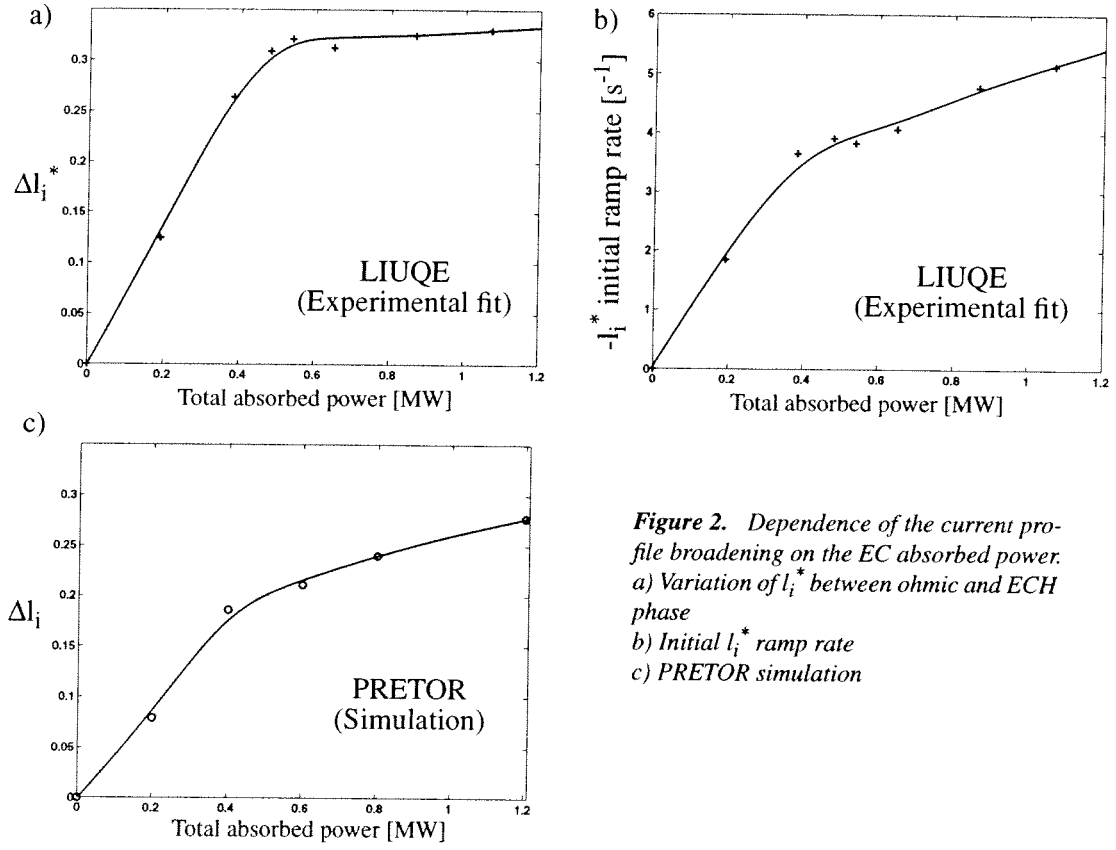


***Figure 2.*** *Dependence of the current profile broadening on the EC absorbed power.*
*a) Variation of $l_i^*$ between ohmic and ECH phase*
*b) Initial $l_i^*$ ramp rate*
*c) PRETOR simulation*

Using the standard parameters described in section 2 and varying the EC power launched, a power scan has been performed. More than 90% of the power launched is absorbed at the first pass.
The current profile broadening effect first increases strongly with the total absorbed power and saturates above $P_{abs}$~0.45 MW. The saturation is more pronounced for the total internal inductance variation between ohmic and ECH phase (Figure 2a) than for the initial $-l_i^*$ ramp rate (Figure 2b) or for the PRETOR simulation (Figure 2c).
At the start of the EC pulse, the normalized deposition radius is set at $\rho$~0.7 for all the shots of the scan. While the current profile is broadening, the elongation increases and the normalized deposition radius decreases. As the deposition radius reaches $\rho$~0.5, the elongation stops increasing, even when applying higher power as shown in figure 2a. In figure 2b, the initial measured $-l_i^*$ ramp rate is by definition insensitive to this effect and in figure 2c the deposition radius was kept constant in the PRETOR simulation. This explains the sharp transition in figure 2a, where the evolution of $\rho_{dep}$ must be taken into account, as compared to figure 2b and 2c.

### 4.2 Deposition width scan

The effect of the width of the deposition location was studied using two launchers : keeping the same average deposition radius ($\rho_{avg}$~0.7), the distance between the two deposition radii $\Delta\rho_{dep}$ was varied from 0 to 0.2.

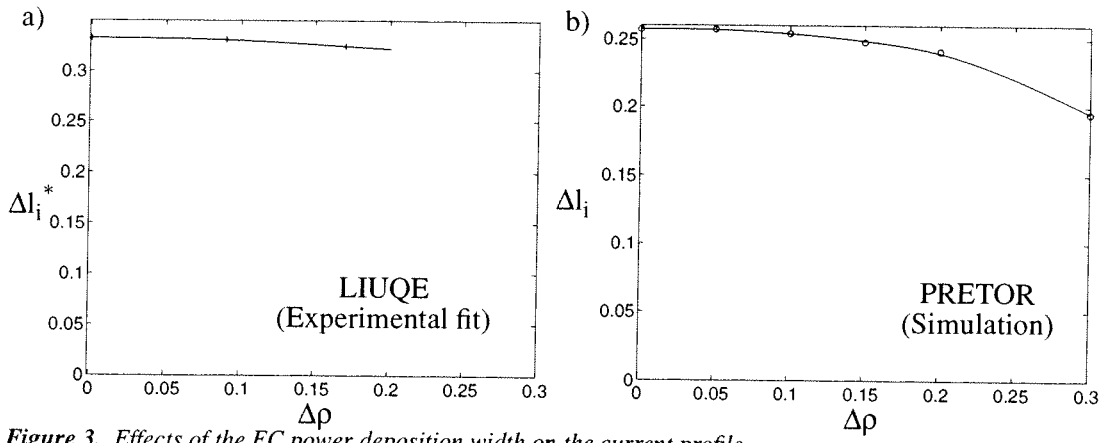


*Figure 3. Effects of the EC power deposition width on the current profile*
*a) Variation of $l_i^*$ between the ohmic and the ECRH phase*
*b) PRETOR simulation*

As shown in the experiment and in the PRETOR simulation the maximum efficiency on the current profile broadening is obtained for the most localized EC power deposition, $\Delta\rho$=0 (Figure 3). The effect of broadening the deposition remains quite small as long as the deposition occurs in the efficient region for current profile broadening. The efficiency decreases significantly when the deposition occurs too far inside (loss of the current profile broadening effect) or too far outside (loss of first pass absorption, reduced confinement).

### 4.3 Toroidal angle scan

The toroidal injection angle $\varphi$ of EC waves was varied from -20° to +20° to study the influence of the EC driven current. Changing the toroidal angle changes the observed current profile and a maximum current profile broadening efficiency is obtained for $\varphi \sim \pm 10°$ (Figure 4). This phenomena occurs both for co-ECCD and counter-ECCD and is consequently not due to the driven current. The calculated current drive efficiency is very low (-2.02 kA/MW at $\varphi$=-20° and +2.64 kA/MW at $\varphi$=+20°) essentially because of the low temperature at the plasma edge (~600 eV).
It appears that some toroidal angle in the co- or in the counter-ECCD direction is interesting for current profile broadening as long as current drive efficiency - and so edge temperature - remains low.

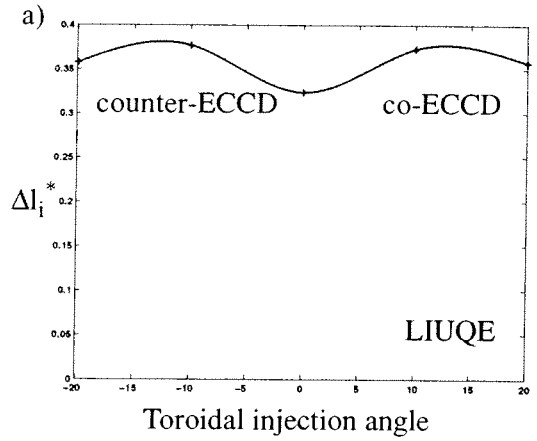


*Figure 4. Effects of the EC waves toroidal injection angle φ on the current profile*

### 4.4 Deposition location scan

The current profile dependence on $\rho_{dep}$ has been evaluated using the TCV database of shots with far off-axis ECH deposition (Figure 5a). Results have been normalized at $I_p$~300kA and $P_{abs}$~1MW to be compared with the PRETOR simulations.
The experimental results show good qualitative agreement with the PRETOR simulations (Figure 5b). The optimal EC power deposition location for broadening the current profile appears to be $0.55<\rho<0.7$ both from experiment and transport simulation.
When the deposition occurs inside $\rho$~0.55, the current profile broadening effect is reduced and become even inverted for $\rho<0.4$ (current profile peaking for the experiment and the PRETOR simulation). On the other hand, for $\rho>0.75$, the deposited EC power is probably no longer well confined and the action on the current profile is reduced.

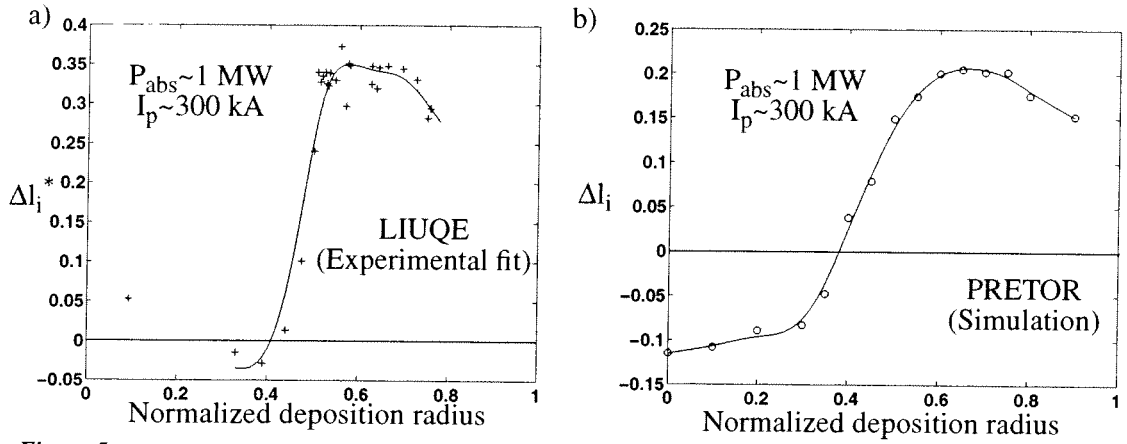


*Figure 5.*
*a) Current profile dependence on the EC power deposition location ρ during the internal inductance plateau. Normalization at $I_p$=300kA and $P_{abs}$=1MW ($0.4<P_{abs}<1.8$MW, $250<I_p<420$ kA).*
*b) PRETOR simulation at Ip=300kA and Pabs=1MW.*

### 4.5 Increasing the density and keeping a constant deposition radius

With fixed launchers, the elongation process saturates when the current profile broadening becomes less efficient, that is typically when the deposition radius reaches 0.5. To flatten the current profile further there are mainly two methods.
The first consists of increasing the plasma density. This increases the first pass power absorption at the plasma edge as calculated by TORAY (Figure 6a) which allows starting the EC power deposition at a more outside deposition location. Increasing the central density from $2.10^{19}$ $m^{-3}$ to $4.10^{19}$ $m^{-3}$ has already allowed us to reach the same final elongation ($\kappa$~2.4) at $I_p$~ 300kA) with ~40% less EC power injected.

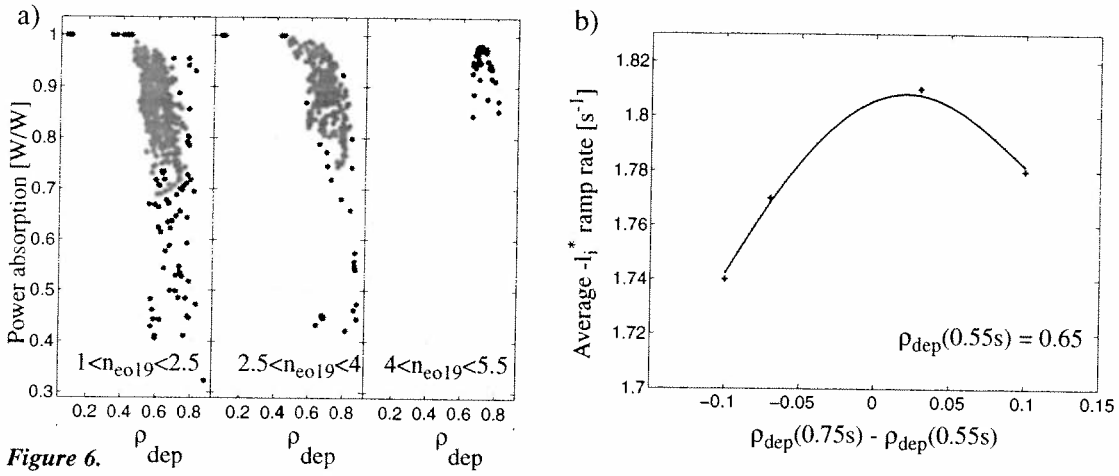


***Figure 6.*** *a) Influence of the density on the edge power absorption calculated from TORAY for the TCV database of off-axis ECH experiments (each point corresponds to one time)*
*b) Variation of the average $-l_i^*$ ramp rate between 0.55s and 0.75s versus power deposition radius changes caused by different mirror speeds*

The second method is to sweep the launcher mirrors during the discharge to keep a constant deposition radius around 0.7. The difficulty is then to follow the plasma elongation evolution, which is not a pre-programmed value. The effect of outward moving deposition was studied by moving the mirrors during the discharge with different speeds. The initial deposition location was $\rho$~0.65 and then increased or decreased depending on the pre-programmed mirror sweep rate relative to the elongation rate. The average $-l_i^*$ ramp rate was shown to increase when the normalized deposition radius was kept approximately constant and was shown to decrease when the deposition became too far inside or too far outside (Figure 6b). In the fixed mirrors case, the average $-l_i^*$ ramp rate between 0.55 s and 0.75 s was 1.7 $s^{-1}$ and keeping $\rho_{dep}$ constant is shown to improve the current profile broadening.
The optimization of such a scenario would require feedback control of the mirrors angles based on plasma elongation and vertical plasma position, to maintain a constant deposition radius. This system is under implementation.

## 5. Conclusions

The maximum current profile broadening efficiency is obtained for a narrow EC power deposition profile with a peak deposition radius between 0.55 and 0.7.
In this scenarios ECCD efficiency is very low (less than 3 mA/W) but a small toroidal angle for the EC wave injection ($\varphi=\pm 10^{\circ}$) allows an increase of the current profile broadening efficiency.
Initial experiments in central overdense plasmas show that increasing the density and keeping a constant deposition radius by steering the launchers have both a favorable effect on current profile broadening efficiency.
Far off-axis ECH power deposition appears to be an effective tool to broaden the current profile and has already allowed the extension of the stable operation domain in TCV. Stable discharges with $\kappa_{max}$=2.45 ($\kappa$>2.4 during the whole plateau) have been created at $I_p$~400 kA with 1.5 MW of injected power.

## Acknowledgment

This work was partly supported by the Swiss National Science Foundation.

## References

[1] Hofmann F. et al., Plasma Phys. Control. Fusion **43** (2001) A161
[2] Pochelon A. et al., Nucl. Fusion **41** (2001) 1663
[3] Hofmann F. et al., European Physical Society Bournemouth Vol 19C Part II (1995) 101
[4] Matsuda K., IEEE Trans. Plasma Sci. **17** (1989) 6
[5] Angioni C. et al., Proc. Theory of Fusion Plasma **ISSP 19** (Varenna 2000) 73

# Exploitation of a Diamagnetic Loop for Modulated ECH Power Absorption Measurements in TCV

A. Manini, J.-M. Moret, S. Alberti, T.P. Goodman and M.A. Henderson

*Centre de Recherches en Physique des Plasmas*
*Association EURATOM - Confédération Suisse*
*Ecole Polytechnique Fédérale de Lausanne, CH-1015 Lausanne*

## Introduction

For the evaluation of the performance of auxiliary heating methods and for the understanding of the transport properties of auxiliary heated plasmas, it is of fundamental importance to determine the fraction of the launched power that is actually transferred to the plasma, as well as where in the plasma the power is deposited. The diagnostic which is probably the best suited for the first goal is the DiaMagnetic Loop (DML) providing a measurement of the diamagnetic flux of the plasma, which is directly related to the total plasma kinetic energy.

TCV is equipped with a very versatile Electron Cyclotron Heating (ECH) system. It consists of six gyrotrons operating at the second harmonic, 82.7 GHz, and three gyrotrons at the third harmonic, 118 GHz. The nominal power for each 82.7 GHz gyrotron is 465 kW and for each 118 GHz gyrotron is 480 kW, resulting in a total of radio frequency power of 4.2 MW. In this paper we present the method that has been developed for determining the absorbed power in the ECH experiments in TCV, pointing out especially the results of the first third harmonic X-Mode (X3) ECH experiments, leaving the problem of the power deposition localisation to other reports [1,2,3]. For the determination of the total plasma kinetic energy, the DML has also been used on other devices such as JET [4], ASDEX [5] and TEXTOR [6], but only for this last case modulation experiments have been performed and analysed.

## Experimental configuration

The launching geometry is shown in figure 1. The X3 wave is launched from the low field side via one of the upper lateral launching antennas normally used for X2 heating [7]. A view of the TORAY-GA ray tracing for the X2 and X3 Radio Frequency (RF) beams is shown. The vertical dashed lines passing close to the plasma magnetic axis correspond to the cold resonances of the respective harmonics. The two resonances are spatially separated by approximately 50 mm and, in the target plasma studied here, they are approximately symmetric with respect to the plasma magnetic axis, the X3 cold resonance being on the low field side. The target plasmas used in the experiments have a major radius $R_0 = 0.88\,\mathrm{m}$, a minor radius $a = 0.25\,\mathrm{m}$, an elongation $\kappa = 1.31$, a toroidal field $B_0 = 1.42\,\mathrm{T}$ and a central electron density $n_{e0} = 2.5 \cdot 10^{19} m^{-3}$. The evolution of relevant plasma parameters is shown in figure 1. The X3 waves are injected in plasmas pre-heated with second harmonic X-mode. The X2 pre-heating is kept at a constant power level from 0.3 to 1.3 s whereas the X3 power is applied from 0.4 to 1.2 s and includes a 150-200 ms phase with 100% power amplitude modulation.

A modulation frequency scan was performed using frequencies between 20 and 700 Hz. It is not useful to use higher values because of the limited DML frequency response and the small signal to noise ratio at higher frequencies. The large variations of the central electron temperature $T_e(0)$, measured by Thomson scattering, are produced by the sawteeth. In this experiment the level of sawtooth activity does not strongly perturb the DML signal. However, in case of strong sawtooth activity, the effect on the DML diagnostic is significantly increased.

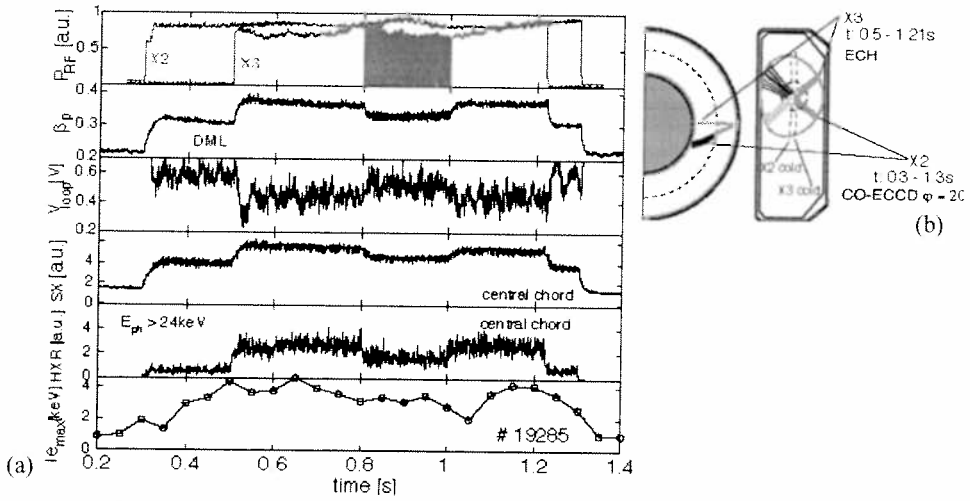


***Figure 1.*** *(a) Typical time traces for the X2 and X3 ECH. From top to bottom: X2/X3 RF power, poloidal beta, loop voltage, soft and hard x-ray signals, electron temperature $T_e(0)$ (measurement taken every 50 ms). RF power: $P_{X2} \sim P_{X3} = 0.47MW$. Plasma current: $I_p = 200kA$, line average density $n_e = 2 \cdot 10^{19} m^{-3}$. (b) Launching configuration for the X3 absorption measurements in presence of X2 pre-heating. The cold resonances of each harmonic (X2 and X3 cold) are indicated by the vertical dashed lines. The circular dashed line in the poloidal plane indicates the reconstructed $q = 1$ surface. The toroidal angle $\varphi$ is defined as $\sin\varphi = \vec{k} \cdot \vec{B} / |\vec{k}||\vec{B}|$, where $\vec{k}$ is the k-vector of the X3 wave and $\vec{B}$ is the magnetic field vector.*

## Analysis procedure

A detailed analysis of the frequency response of the DML and of the relationship between the modulation of the diamagnetic flux of the plasma and its energy are described in detail in [8]. We will here focus on the modelling of the power balance equation. Since the electron temperature is much higher than the ion temperature, and since the electron density is rather low (X2 cut off!), we can neglect the contribution of the ions. This will not be possible for pure X3 heating at higher densities, where the two temperatures are also closer [9].

The analysis procedure can be divided into two different parts. In a first step the power balance equation is analysed, which allows the determination of the experimental requirements for the modulation frequency. In the second step, the plasma energy response to the injected ECH power modulation is extracted. Hence, the decomposition of the signals allows the determination of the absorbed power as well as the phase difference between the modulated DML energy and the ECH reference signal. The power balance equations in the perpendicular and parallel directions are given by

$$\frac{dW_{\parallel}}{dt} = -\frac{W_{\parallel}}{\tau_{inc}} + \frac{1}{\tau_{ed}}\left(\frac{1}{2}W_{\perp} - W_{\parallel}\right) \tag{1}$$

$$\frac{dW_{\perp}}{dt} = -\frac{W_{\perp}}{\tau_{inc}} + P - \frac{1}{\tau_{ed}}\left(\frac{1}{2}W_{\perp} - W_{\parallel}\right) \tag{2}$$

The term P contains the power source which directly increases the perpendicular energy, which in our case is all the additional ECH power [10], $\tau_{inc} = dW/dP$ is the incremental energy confinement time as defined in [6], $\tau_{ed}$ is the electron deflection time which determines the time in which an anisotropy of the plasma (given by the term $1/2W_{\perp} - W_{\parallel}$) can be maintained in the presence of pitch angle scattering. The total plasma energy is given by $W = W_{\parallel} + W_{\perp}$. Equations (1) and (2) are expressed using the same $\tau_{inc}$ for both the

parallel and perpendicular energies. In principle, though, the perpendicular and parallel $\tau_{inc}$ could be different. Such a difference, though, should be taken in consideration only for the cases in which $\tau_{inc} \to \tau_{ed}$: in fact, if $\tau_{inc} \gg \tau_{ed}$, the isotropisation of the plasma is much faster than the energy relaxation, which directly leads to the same $\tau_{inc}$ for the two directions. It can be shown that $\tau_{inc}$ is in fact much larger than $\tau_{ed}$ (see [8]).

Assuming a fully isotropic plasma, i.e. if $\tau_{ed} \to 0$ and $1/2 W_{\perp} - W_{\parallel} \to 0$, then equations (1) and (2) can be simplified, after Fourier transformation, to

$$\tilde{W} = \frac{1}{i\omega + 1/\tau_{inc}} \cdot \tilde{P} \equiv H \cdot \tilde{P}, \tag{3}$$

where H is the transfer function so defined. Hence, if the modulation frequency is large enough that the energy losses in one cycle can be ignored, i.e. if

$$\omega \tau_{inc} \gg 1, \tag{4}$$

then we obtain

$$\tilde{W} = -\frac{i}{\omega}\tilde{P}. \tag{5}$$

This simple relationship is valid for any frequency satisfying (4) but only for a fully isotropic plasma. Now, having the possibility of deriving $\tilde{W}$ from the DML, we can then determine the injected power. The calculation reduces to multiplying the modulation contribution to the plasma energy by the modulation frequency, $|\tilde{P}| = \omega \cdot |\tilde{W}|$, with the phase difference between the energy modulation contribution and the injected power modulation contribution being $90°$.

The more realistic case, in which both the incremental energy confinement time $\tau_{inc}$ and the pitch angle scattering time $\tau_{ed}$ have to be considered, has been analysed in [8], demonstrating the validity of the assumptions of plasma isotropy for these experiments.

**Application of the DML estimate to X3 absorption measurements**

These experiments were aimed at establishing the influence of the plasma conditions on the absorption of X3 ECH power. The plasmas were pre-heated with different power levels of X2 ECH and ECCD. In particular, the X3 power (0.47 MW) and its toroidal launching angle were kept constant, while different X2 conditions were investigated including variations of the toroidal launching angle, of the power deposition radius and of the total X2 power. For studies of single pass absorption the poloidal angle of the X3 beam was swept in the poloidal plane. For all these cases, the absorbed power is estimated during the modulated portion of the X3 pulse.

*X3 Absorption versus X2 pre-heat power*

Figure 2 (a) shows the X3 absorbed power fraction versus the X2 pre-heat power for three X2 launching angles corresponding to central CO-ECCD, ECH and CNT-ECCD. For the three different X2 launching conditions a fit of the global energy confinement time to the injected power of the form $\tau_E = A P^{\alpha_p}{}_{in}$, yields $A = 4.4 \cdot 10^{-3}$, $\alpha_p = 0.75 \pm 0.1$. This is consistent with a previous global energy confinement time scaling [11]. For all these discharges, the measured phase difference between the modulated injected power and the energy modulation was $90° \pm 10°$, consistent, within the experimental error bars, with (5) under the condition given by (4). For CO-ECCD target plasmas full single-pass absorption was obtained.

The absorption calculated with the TORAY-GA code [12], is compared with the measured one in figure 2 (b). The absorption is systematically higher than the TORAY-GA

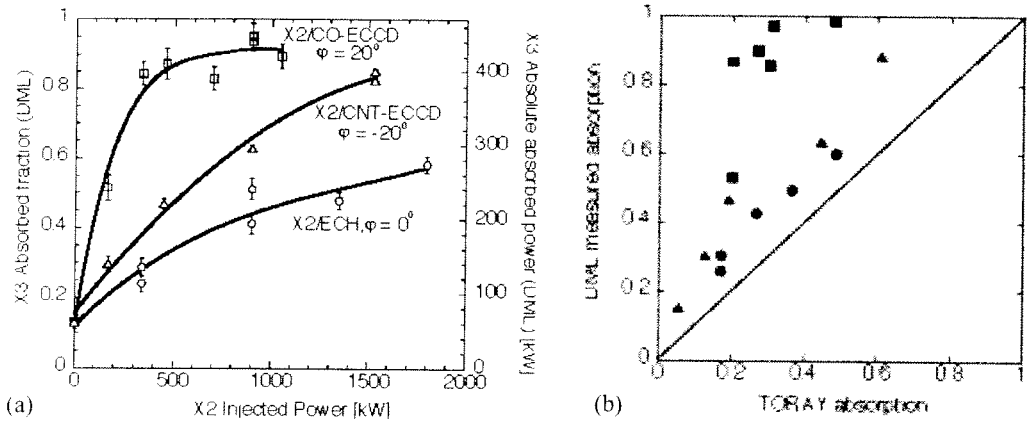


*Figure 2. (a) Measured X3 absorption using the DML versus the X2 pre-heat power for three different X2 launching configurations: CO-ECCD (φ = 20°), CNT-ECCD (φ = −20°) and ECH (φ = 0°). The X3 injected power was kept constant at 0.47MW with central deposition and zero toroidal injection angle (ECH). The target plasma is shown in figure 1. (b) Measured X3 absorption versus calculated absorption with the TORAY code for the shots shown in figure 1. The three different symbols correspond to the following X2 pre-heatings: triangles → CO-ECCD, squares → CNT-ECCD and circles → ECH.*

predictions, with the largest discrepancy occurring for the CO-ECCD case which shows a difference of up to a factor of 3.

*X3 single-pass absorption*

An exploration for the estimation of the effect of any second-pass absorption is made by a poloidal scan of the launching angle (from central to off-axis, $r/a > 0.5$) while keeping the X2 beam fixed; the X2 toroidal injection angle is set at φ = 20° in CO-ECCD (see figure 3). This is complemented by a polarisation scan of the X3 beam. The poloidal beta is estimated using the DML. The hard X-ray signals are measured with an energy resolving camera [13] and the traces shown correspond to a central chord with different energy filters. The high-field side radiometer (HFS-ECE) [14] views the plasma magnetic axis. Both the hard X-ray diagnostic and the HFS-ECE are sensitive to supra-thermal electrons, whereas the poloidal beta is related to the global plasma energy variation. The radiometer signal is calibrated against $T_e(0)$ during the ohmic phase.

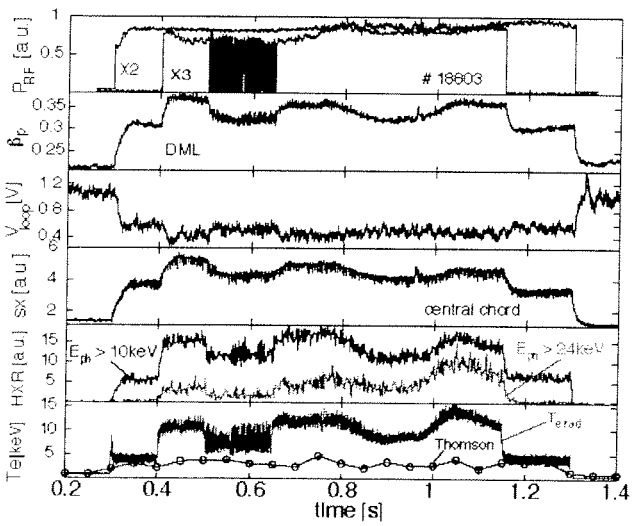


*Figure 3. From top to bottom: RF power for X2 and X3, poloidal beta, loop voltage, soft X-ray, two hard X-ray signals for different photon energy ranges, central electron temperature, radiation temperature measured by high-field-side radiometer.*

In these discharges the evolution of the X2 and X3 powers is similar to the one shown in figure 1 up to 0.7s, after which the X3 beam is moved up. The X3 beam trajectory at three different times ((a) t<0.7s, (b) t=0.9s and (c) t=1.1s) is shown in figure 4 (a). As the X3 beam is moved off axis, a clear decrease followed by an

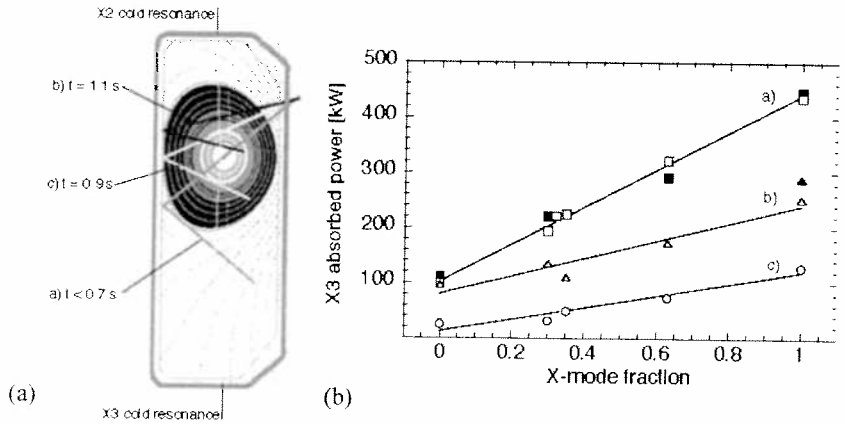


***Figure 4.*** *(a) Poloidal scan of the X3 RF-beam with X2 pre-heating at φ = 20° (CO-ECCD). Only the central ray trajectory of the X3 beam is shown for three times: (a) t<0.7s, (b) t=0.9s and (c) t=1.1s. (b) X3 absorption versus X-mode fraction. The filled symbols indicate absorption measurements with the DML, whereas the open symbols are absorption measurements inferred from the variation of the soft X-ray signal, $\Delta I_{sxn}$. The three curves correspond to: (a) central injection (t< 0.7s), (b) second pass high-field side absorption (t=1.1s), and (c) off-axis injection (t=0.9s). The filled triangle is an absorption measurement with the DML for high-field side absorption. The continuous lines are linear fits of the $\Delta I_{sxn}$ signals.*

increase of the beta poloidal, hard X-ray and HFS-ECE signals is observed from 0.8s to 1.1s. This signal structure can be explained by the fact that, for a Maxwellian distribution function, the X3 optical depth is proportional to the small term $(k_B T_e / m_e c^2)^2$ [15] and as the beam moves away from the region of highest temperature, the optical depth is strongly decreased with an associated weaker absorption. At t=1.1s, the launching angle is such that the beam is reflected by the graphite tiles of the central column and the reflected beam reaches the region of highest temperature on the plasma axis, where efficient absorption again occurs, but from the high field side and with a somewhat less focused beam. For all other times, the beam suffers multiple reflections inside the vacuum vessel and the RF power is eventually absorbed on the vessel walls or partially lost through the different apertures with only a negligible amount absorbed on the X3 resonance layer.

A more quantitative study of the multi-pass absorption has been attempted by varying the X-mode fraction of the injected X3 beam. The X-mode fraction is controlled by a grating polariser in a matching optics unit located at the gyrotron output. Since, for a Maxwellian distribution function, the optical depth of the O-mode fraction is proportional to $(k_B T_e / m_e c^2)^3$ [15], the absorption of this mode is practically zero.The soft X-ray emission viewed on a central chord divided by the line average density follows a similar behaviour as the stored energy variation in the plasma [16]. To use the $\Delta I_{sxn}$ signal, $\Delta I_{sxn}$ being the variation of the soft x-ray emissivity at the turning on of the X3 power, as a measurement of the absorbed power, it is calibrated against the DML for one point of figure 4 (b), where both measurements, DML and $\Delta I_{sxn}$, are available. Curve (a) shows the variation of $\Delta I_{sxn}$ at X3 turn-on superposed on the DML absorbed power versus X-mode fraction. Curve (b) (second pass high field side absorption), only shows the $\Delta I_{sxn}$ variation versus X-mode fraction with one point measured with the DML (at 100% X-mode). Again good agreement between $\Delta I_{sxn}$ and the DML measurement is found where both measurements are available. Finally curve (c) shows $\Delta I_{sxn}$ versus X-mode fraction for the case of off-axis injection(t=0.9s) with a ray trajectory missing the plasma centre on first and second pass. This last curve shows that, as the beam misses the plasma axis, the multi-pass absorption is negligible (<5%). For central first-pass deposition or second-pass high field side deposition, the relatively high absorption

(~20%) in pure O-mode might be associated with the presence of a supra-thermal tail in the electron distribution function generated by the X2 pre-heating [17]. For X-mode central deposition, this study demonstrates that only single pass absorption is being measured.

## Conclusion

Modulated ECH has been used to determine the ECH X2 and X3 power absorption from the measurement of the diamagnetic flux variations using the DML. Since only the modulation contribution is relevant to the analysis, the method does not require a perfect compensation of the diamagnetic flux measurement, although a good compensation of the vessel poloidal image current is crucial for ensuring a sufficiently large bandwidth to allow the use of high frequency modulation. The analysis of the behaviour of the amplitude and phase response in the modulation frequency scan has demonstrated the validity of the power absorption calculations with respect to the measured energy confinement time and the pitch angle scattering time. The method has been applied to the study of the absorption of the X3 ECH under different X2 pre-heat scenarios. The variations of amplitude and phase as a function of frequency, compared with different models, confirms the validity of the measurements. It has been demonstrated that single-pass absorption of the X3 is measured for central X3 injection with a X2 pre-heating in CO-ECCD, where only 55% absorption is predicted by the ray tracing code TORAY. The discrepancy is explained by the presence of an energetic electron tail generated by the X2 pre-heating. The presence of this tail is confirmed by hard x-ray photon spectra and by a high filed side ECE radiometer. The next step will consist of performing experiments at higher densities using the vertical X3 launcher of TCV.

## Acknowledgment

This work was partly supported by the Swiss National Science Foundation.

## Bibliography

[1] D.J. Gambier *et al* 1990 *Nucl. Fusion* **30** 23
[2] E. Barbato and R. Giannella 1985 *Phys. Lett.* A **110** 309
[3] A. Manini *et al CRPP Internal Report* LRP 664/00
[4] G. Tonetti *et al* 1986 *Rev. Sci. Instrum.* **75** 2087
[5] J. Gernhardt and F. Schneider *IPP Report* No. III/84
[6] D. Lebeau *et al* 1995 *Plasma Phys. Control. Fusion* **37** 1141
[7] T.P. Goodman *et al* 1997 *Proc. 19th Symp. on Fusion Technology (Lisbon, 1996)* ed C. Varandas and F. Serra (Amsterdam: North-Holland) p 565
[8] A. Manini *et al* 2002 *Plasma Phys. Control. Fusion* **44** 139
[9] G. Arnoux *et al* Poster P-2.076 of *29th EPS Conference* (Montreux, 17-21 June 2002)
[10] V. Erckmann and U. Gasparino 1994 *Plasma Phys. Control. Fusion* **36** 1869
[11] A. Pochelon *et al* 1999 *Nucl. Fusion* **39** 1807
[12] G.R. Smith *et al* 1995 *Proc. 9th Joint Workshop on ECE and ECRH (Borrego Springs, CA)* (Singapore: World Scientific) p 651
[13] S. Coda *et al* 2001 *Proc. 28th EPS Conf. on Controlled Fusion and Plasma Physics (Madeira, Portugal)* p1.075
[14] P. Blanchard et al 2001 *Proc. 28th EPS Conf. on Controlled Fusion and Plasma Physics (Madeira, Portugal)*
[15] M. Bornatici *et al* 1983 *Nucl. Fusion* **23** 1153
[16] M.A. Henderson *et al* 2001 *Fusion Eng. Design* **53** 241
[17] S. Alberti *et al* 2002 *Nucl. Fusion* **42** 42

# Preliminary results of top launch 3rd harmonic X-mode Electron Cyclotron Heating in the TCV Tokamak

J.-P. Hogge,* S. Alberti, L. Porte, and G. Arnoux
*Centre de Recherche en Physique des Plasmas,*
*Association Euratom-Confédération Suisse,*
*Ecole Polytechnique Fédérale de Lausanne,*
*CH-1015 Lausanne, Switzerland*

The ECH system on TCV has recently been upgraded to a total of 4.5MW of installed power. In order to extend the density range of ECH heated plasmas up to electron densities of $1.2 \times 10^{20}\mathrm{m}^{-3}$, three 0.5MW gyrotrons at a frequency of 118GHz have been added to the existing 3MW 2nd harmonic system operating at a frequency of 82.7GHz. The launcher consists of 1 mirror placed at the top of the vessel, which collects the power of the 3 microwave sources, and can be steered radially and poloidally to ensure maximum flexibility. The choice of the top-launch scheme results as a compromize between heating of high density plasmas and the maximisation of single-pass absorption in ohmically heated target plasmas. In this launching configuration, the high sensitivity of single-pass absorption on launching geometry has been experimentally demonstrated. A comparison between the experimental results and the linear ray-tracing/absorption code TORAY-GA shows a good agreement for densities up to $6.0 \times 10^{19}\mathrm{m}^{-3}$.

## I. INTRODUCTION

In the past decade, electron cyclotron waves (ECW) have proven a highly efficient tool for localized heating (ECRH), current drive (ECCD) [1], MHD activity control [2] or plasma breakdown in magnetically confined plasmas. In addition, the relative simplicity of the launching system and the insensitivity of the wave propagation to the plasma boundary location make ECW the most appropriate additional heating scheme for the wide variety of plasma shapes produced by TCV.

On TCV, a first set of six gyrotrons emitting a total of 3MW at 82.7GHz (X2), close to the second harmonic of the cyclotron frequency $\Omega_{ce}$ was installed by the end of the nineties and has operated ever since. Each X2 gyrotron has its own launcher located on the low field side (LFS) either on the upper plane or on the equatorial plane. The antennas are designed in such a way that the radiation can be directed almost anywhere in a cone with an opening angle of 110 degrees, allowing to set the deposition location with a high accuracy. The cutoff density for the X2 wave is given by $n_{cx_2} = 4.2 \times 10^{19}\mathrm{m}^{-3}$. In order to increase the range of accessible densities, the ECH system was upgraded by an additional set of 3 0.5MW/118GHz gyrotrons intended to heat the plasma at the third harmonic extraordinary mode (X3), which has a cutoff density $n_{cx_3} = 1.2 \times 10^{20}\mathrm{m}^{-3}$.

Initial X3 experiments, in which one LFS X2 launcher was used to inject the 3rd harmonic in a plasma preheated with 2nd harmonic injection were performed [3]. It was shown that X2 preheating in co-current drive and the subsequent departure of the distribution function from a Maxwellian could lead to single-pass full absorption of the X3 power.

In the final configuration, the power generated by each tube will be transmitted to TCV by means of an evacuated corrugated waveguide transmission line and all the radiation will be gathered and directed onto a single mirror placed at the top of the vessel. So far, two X3 top-launch transmission lines are in use, whereas the option of using an upper lateral LFS launcher for the last tube has been kept.

In this paper, we report the injection of 1.5MW of X3 power in TCV for the first time. These experiments were dedicated to the commissioning of the complete X3 heating system and no X2 preheating was present.

In section II, the transmission line system and the launcher antenna are presented. Initial experimental results are given and discussed in section III , and a comparison with the predictions of the linear ray tracing/absorption code TORAY-GA [4–6] is made.

## II. THE X3 TRANSMISSION LINES

A sketch of the X3 transmission line system is given in figure 1. The RF beam of each gyrotron is individually coupled into an evacuated $HE_{11}$ transmission line via a matching optics unit (MOU). The gyrotron and MOU are described in II A. The waveguide transmission lines are similar to the X2 system and are discussed in II B. In paragraph II C, emphasis is put on the launcher antenna which was designed, built and installed for this project.

### A. Gyrotrons and MOU

The 118GHz gyrotron development for TCV and Tore Supra was performed within the frame of a joint development between the Associations Euratom-CEA, Euratom-Confédération Suisse, Euratom-FZK and Thalès Electron Devices.

The design output power is 500kW for a pulse length of 210s (2s pulses at Lausanne) and this tube has achieved 300kW during 111s [7], corresponding to the world record of output energy per pulse of 33MJ at the time it was reported. The tube has been extensively described in [8],

*Electronic address: jean-philippe.hogge@epfl.ch

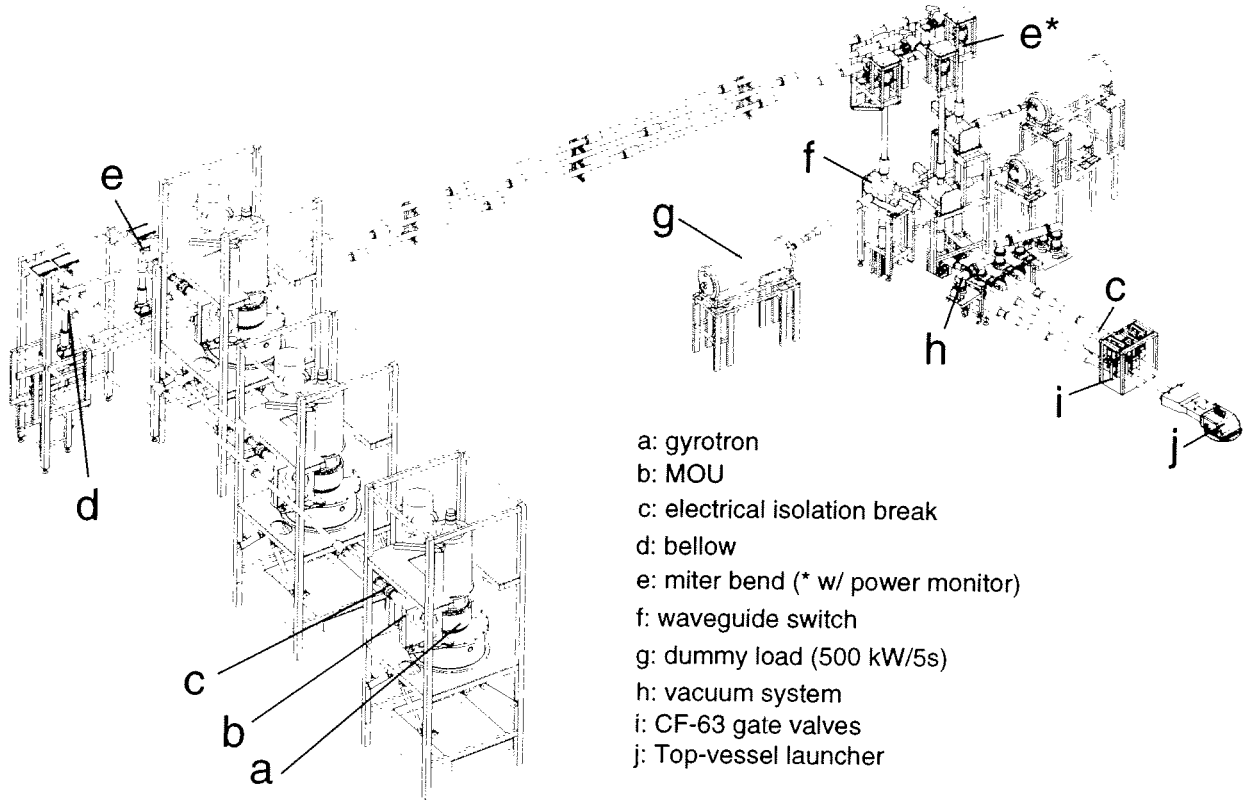


FIG. 1: Picture of the 118GHz gyrotron.

TABLE I: Typical operation parameters of the gyrotrons

| Parameter | Experimental value |
|---|---|
| Ouput power | 500kW |
| Pulse length | 2s |
| Operating mode | $TE_{22,6}$ |
| Frequency | 117.77GHz |
| Accelerating voltage $V_b$ | 81.5kV |
| Mod-Anode voltage $V_a$ | 24.8kV |
| Beam current $I_b$ | 22A |
| Cavity magnetic field $B_o$ | 4.67T |
| Electronic efficiency (soft excitation) | 33% |
| Window material | Sapphire @ 77K |
| Waist of $TEM_{0,0}$ @ window | $w_{0x} = 22.6$mm |
| | $w_{0y} = 27.3$mm |
| Mode purity @ window | 95.8% |
| Overall Gyrotron efficiency in $HE_{1,1}$ mode | 28% |

its main operating parameters of the tube are summarized on table I.

Modulation of the RF power is achieved by tuning the Mod-Anode voltage. In the experiments reported here, on/off modulation was used. A drop $\Delta V_a = 3.5$kV would terminate the oscillation.

The Matching Optics Unit consists of a universal polarizer made by 2 gratings and an elliptical mirror which compensates for the beam astigmatism and matches the $TEM_{0,0}$ mode to the the fundamental $HE_{1,1}$ mode of the corrugated waveguide.

### B. Corrugated transmission line

For the sake of compatibility with the existing X2 transmission lines system, all the components (except for the power monitor miter bends) were designed and manufactered by General Atomics (USA) and Spinner GmbH (Germany) so that they could be used at both 82GHz and 118GHz. The corrugated $HE_{11}$ waveguide has a diameter of 63.5mm and is in Aluminium. A typical line is very similar to those of the X2 system [9] and consists of:

- Electrical isolation breaks to isolate the line from the MOU and from TCV,
- Bellows to compensate for any thermal expansion,
- Sections of straight waveguide (max. 2.1m),
- Miter bends with planar copper reflectors. Some of them are equipped with a -80dB coupler to monitor the forward and reverse power,
- A microwave switch which can direct the radiation toward the plasma or to a 500kW/5s water load used to calibrate the power monitors and to operate the gyrotron in the absence of plasma,
- A tee is connected to a pumping group (each line is pumped in the MOU and close to TCV),
- A CF-63 gate valve,
- A section of stainless steel waveguide which is connected to the launcher.

The overall transmission line efficiency is estimated to be higher than 95%.

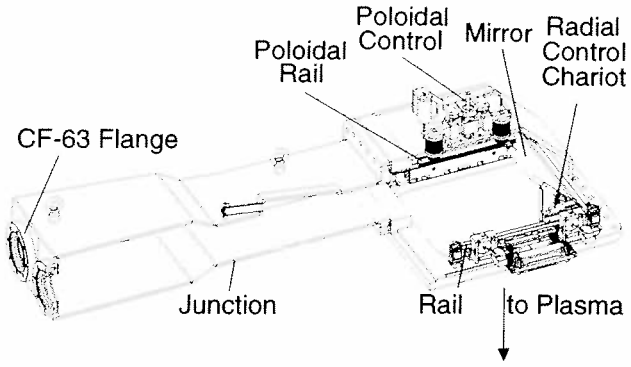


FIG. 2: Schematic of the top-launcher antenna

### C. Antenna launcher

Due to the lower optical depth compared to X2 heating, it was decided to launch the X3 waves from the top of the vessel in order to maximize the ray path in the resonance layer. For the same reason, driving current with the X3 appears unfeasible. A launcher was designed and installed on TCV and is depicted on figure 2.

The three transmission lines converge at an angle of 4 degrees toward a point which is close to the vessel center. The last section of waveguide is in stainless steel to be compatible with the baking temperature of TCV and has a slightly lower diameter (59.2mm) so that standard CF-63 flanges can be used. They are connected to the launcher by means of a junction piece and the waveguide apertures are located further inside to keep the RF beam size compatible with the geometrical constraints of the launcher.

All the radiation is collected by a toroidal mirror and focused into the plasma, close to the equatorial plane. The radii of curvature were chosen so as to minimize the variation of the image beam dimensions versus the mirror radial position. The mirror is made of OFHC copper and does not require cooling. The non-normal incidence of the external beam on the mirror gives rise to a slight toroidal component of the reflected rays, as well as to some aberrations. These two effects were not explicitely taken into account but are assumed to be of second order as their importance is proportional $\tan^2\theta_i \left(\frac{w_m}{f}\right)^2$ where $\theta_i$ is the incidence angle, $f$ the focal length and $w_m$ the beam spot-size on the mirror [10].

The mirror can be steered poloidally during a plasma shot and radially between shots. To ensure the radial motion, the mirror is placed on a chariot which is itself rolling on two parallel rails. Two chains are fixed on the chariot and transmit the external torque via a rotating feedthrough. The poloidal steering mechanism relies on a horizontal rail which can be moved up and down. The top part of the mirror is connected to the rail and can slide along it. It is also attached to the chariot with a pivot which allows a slight rotation around the main axis without any play. A vertical motion of the rail results in a change of the incidence angle on the mirror.

Figure 3 represents a poloidal view of the vessel, with typical plasma flux contours and the (idealized) rays issued from the top-launcher in two extreme configurations. The radial motion of the launcher is limited by the available room. Also depicted is the upper lateral LFS launcher that is shared by X2 and one X3 gyrotron.

The most noticeable differences between the X3 top-vessel and X2 side launchers are – except for the simpler design – the fact that the X3 launcher does not allow any toroidal steering, and that the RF beams converge into the plasma (the X2 beams are in general divergent

TABLE II: Launcher characteristics

| Parameter | Value |
|---|---|
| Dimensions | 250 x 180mm$^2$ |
| Radial motion w/ respect to TCV axis | 800–970mm |
| Radial motion speed (between shots) | 50mm/s |
| Poloidal motion range | $\pm 5^o$ |
| Poloidal motion speed | $10^o$/s (min) |
| Material | OHFC copper |
| Average $\Delta T$ for a 1.5 MW/2s pulse | $12^o$C |
| Maximal $\Delta T$ for a 1.5 MW/2s pulse | $150^o$C |
| Distance waveguide – mirror | 630 – 800mm |
| Distance mirror – plasma focus | 550 – 950mm |
| Waist of the output beam | 29 – 30mm |
| Convergence angle of output beam | $1.5^o$ |
| Curvature radii in hor./vert. planes | 1980/990mm |
| Focal length of the mirror | 700mm |

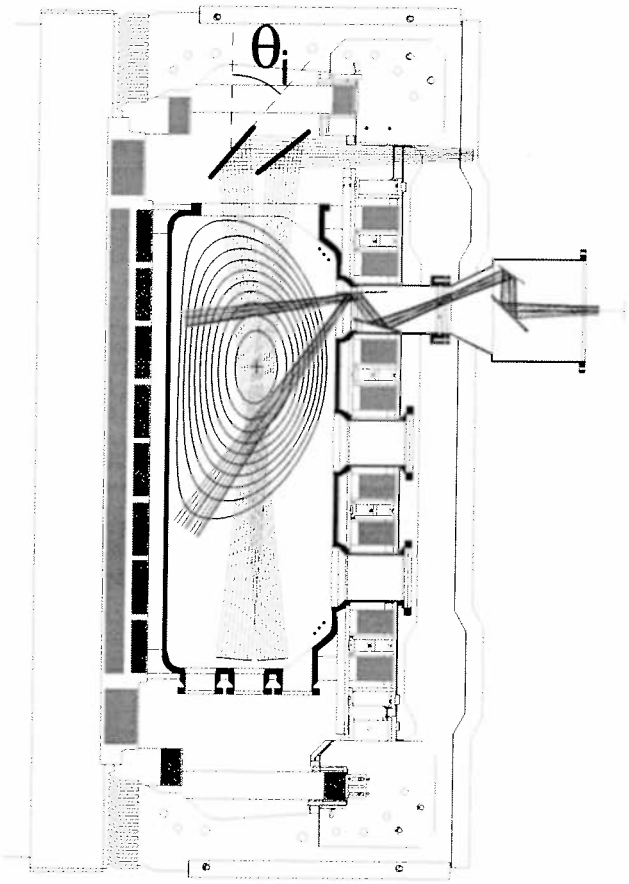


FIG. 3: Sketch of the accessible domains with the X3 top launcher and with an upper lateral launcher.

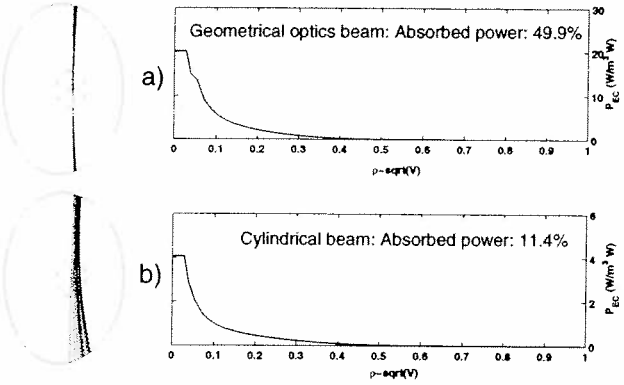


FIG. 4: Simulation of the ray trajectories with a) a converging beam, b) rays distributed on a cylinder. The plasma parameters are: $n_{e_{max}} = 5. \times 10^{19}\mathrm{m}^3$, $B_0 = 1.44\mathrm{T}$, $I_P = 200\mathrm{kA}$, $T_e = 1.1\mathrm{keV}$ (shot # 21374)

as they reach the plasma boundary).

Since the RF beam issued from the launcher converges into the plasma, attention must then be paid to the ray distribution used simulate the absorption in TORAY-GA. In particular, it must be noticed that the usual geometrical optics description, in which the rays are perpendicular to the wavefront at the interface vacuum-plasma leads to rays that would converge to a point focus in the absence of plasma, which is obviously inaccurate. Another possible description consists in distributing the rays on a cylinder having the minimal spot-size radius. In order to illustrate the importance of an appropriate rays distribution, two TORAY-GA simulations are compared on figure 4. In the first case the rays converge to the center of the plasma, whereas they are parallel in the second case. The ratio of the simulated absorbed power is larger than 4.

All the simulations presented further were made with a cylindrical beam.

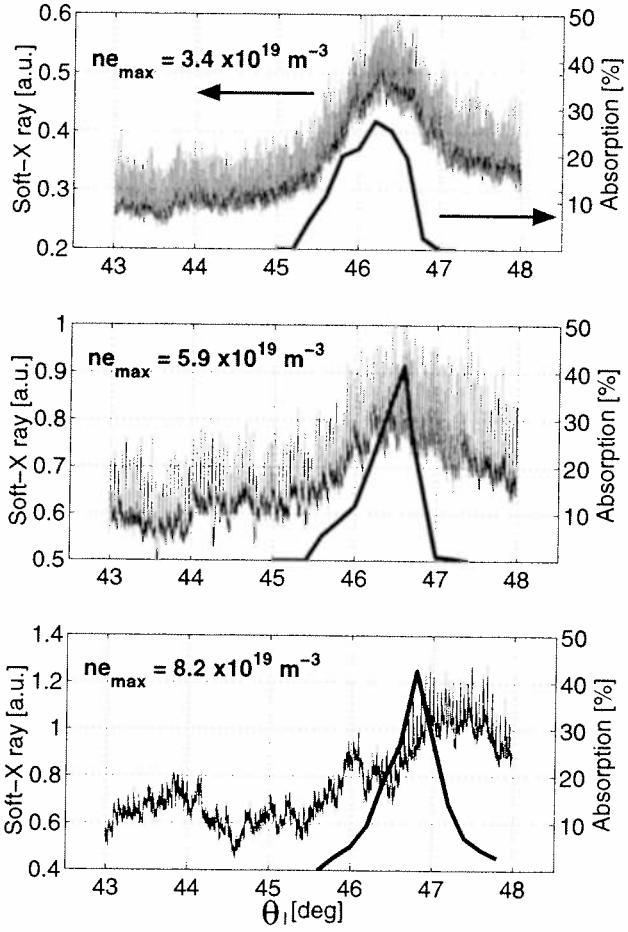


FIG. 5: A central SXR camera plotted with the TORAY-GA absorption prediction as a function of the launcher poloidal angle $\theta_i$ (angle between the mirror plane and a vertical line, $\theta_i = 45^0$ corresponds to a vertical injection), for different plasma densities. Increased SXR signal indicates an increased absorption.

## III. PRELIMINARY RESULTS

The X3 heating system with top-launch has been installed on TCV and commissionned. In the present configuration, 1MW is launched from the top, while one of the LSF upper lateral launchers is shared by an X2 tube and the remaining 0.5MW of X3.

The experiments presented here were mainly dedicated to the commissionning of the X3 system and to the assessment of the sensitivity of the plasma response to the launcher position. In order to isolate the effects of the third harmonic heating, no X2 preheating was present. No attempt was yet made to optimize the performance of X3 heating.

The injected power was stepped from 0.5MW (1 gyrotron, top launch) to 1.5MW (3 gyrotrons: 2 top launch + 1 LFS). Sweeps of the poloidal angle were realized at different radial position and the density was scanned up to $n_{e_{max}} = 8.5 \times 10^{20}\mathrm{m}^{-3}$, far above the X2 cutoff density.

It was possible to measure the absorbed power by modulating the X3 power (on/off modulation at a frequency $\nu_{\mathrm{mod}} = 237\mathrm{Hz}$) and by measuring the response of a diamagnetic loop (DML) [11].

The typical shot parameters were: large radius $R = 0.88\mathrm{m}$, minor radius $a = 0.25\mathrm{m}$, plasma current $I_P \simeq 400\mathrm{kA}$, $n_{e_{max}} = 3. - 8.5 \times 10^{19}\mathrm{m}^3$, $T_{e_{ohm}} \simeq 1\mathrm{keV}$, elongation $\kappa \simeq 1.8$, triangularity $\delta \simeq 0.1$, $q_{edge} \simeq 3$, $B_0 = 1.41 - 1.44\mathrm{T}$.

Figure 5 shows a comparison of an SXR camera signal with the absorption predicted by TORAY-GA, for three different plasma densities, as a function of the poloidal injection angle. For these shots, the radial position of the mirror was $R_{mirror} = 0.935\mathrm{m}$ whereas the cold third harmonic resonance was located at $R_{X3} = 0.88m$. A good qualitative agreement is found, both in the localization of the highest absorption and the sensitivity to the launcher angle, but it appears to deteriorate as the density increases.

It is also seen that signal amplitude variation increases with the density, which suggests that the absorption is improved at higher density, as predicted by the theory.

Another feature which appears clearly on figure 5 is the

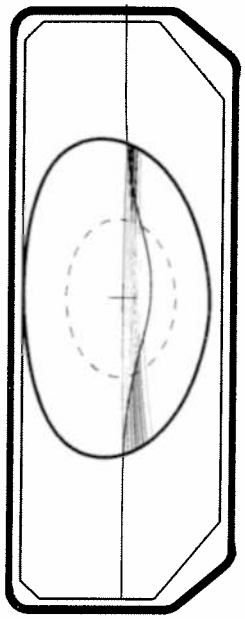

FIG. 6: Ray trajectories predicted by TORAY-GA, shot #22220 at time t=1.05s. The location where absorption occurs are greyed and the cold resonance is represented.

narrow range of launcher poloidal angles giving rise to a reasonable absorption. This effect is due to the shallow incidence angle, and to the fact that a small modification of the refractive index may significantly influence the ray path.

Typical ray trajectories simulated by TORAY-GA are shown on figure 6 for a shot with a maximal central density $n_{e_{max}} = 4.2 \times 10^{19}\mathrm{m}^3$. Also depicted on the same plot is the third harmonic cold resonance and the ray locations where absorption occurs (greyed portion of the paths).

The delocalized character of the absorption appears clearly on figure 7 which gives the absorbed power density as a function of the normalized radius, for the same shot. The typical range of absorption extends over $\rho = 0.1 - 0.6$.

Due to the sensitivity of the ray trajectories to the density profile in this launching configuration, central absorption has been marginally observed. More than refraction of the rays, this effect is due to the relative location of the resonance layer with respect to the center. The paramagnetic effect shifts the layer further away from the center, and an adjustment of the magnetic field may be necessary if absorption at the center is needed (compare figures 4 and 6; the main differences lies in the magnetic field and the plasma current).

Thomson profiles are shown on figure 8, before and during the ECRH phase. The density profile is not affected by ECRH.

The TORAY-GA prediction of the total absorbed power was shown to be consistent with the DML measure. In an unoptimized discharge, TORAY-GA predicts 51% first pass absorption, whereas the DML indicates 220±30kW, for an injected power of 450kW. The larger

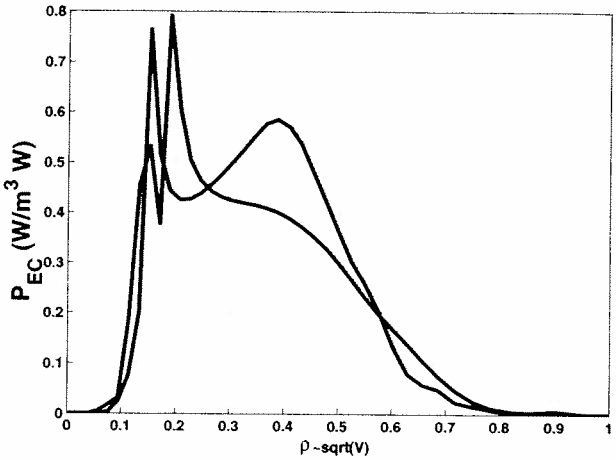


FIG. 7: Absorbed power density as a function of the normalized radius. The curves correspond to the two top-launched beams. Shot #22220 at time t=1.05s.

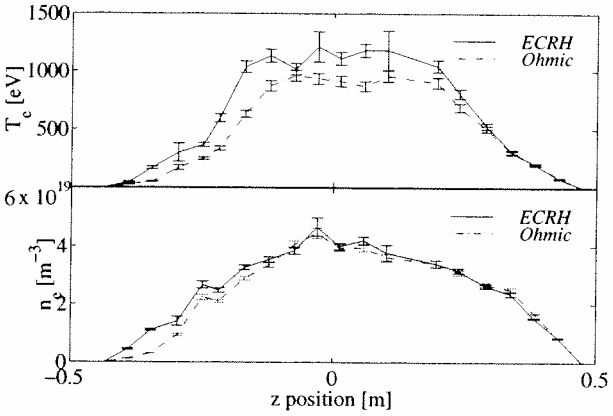


FIG. 8: Thomson temperature and density profiles before and during ECRH. Shot #22220 at times t=0.4 and 1.05s.

densities at which the X3 heating is intended to operate give rise to an improved coupling beetween electrons and ions and they should be taken into account.

## IV. CONCLUSION AND FUTURE PROSPECTS

The third harmonic heating system has been installed and commissionned on TCV It has been possible to launch the 3 RF beams in a temporary configuration (2 beams on top launcher + 1 beam on LFS).

It has been demonstrated that TORAY-GA gives accurate predictions in terms of the absorbed power as well as ray trajetories at low and moderate densities. However, the agreement deteriorates as the density increases and further experiments are needed understand the cause of this effect. The absorbed power is corroborated by DML measurements. The DML model has to be improved to include the electron-ion coupling.

Due to the launching geometry, the system is very sen-

sitive to the plasma profile. It appears therefore desirable to implement a system that could account for profile changes and optimize the launcher poloidal position in real time. This is particularly desired in the optics of using X3-ECRH to heat H-mode plasmas.

It has also been demonstrated that the geometrical approach to describe the ray bundle is not appropriate if the RF beam is convergent into the plasma. A collaboration with ENR-Milano to use a quasi-optical approach (beam tracing) [12] is underway.

### Acknowledgments

The work at CRPP is partially supported by the Swiss National Science Foundation.

[1] V. Erckmann, and U. Gasparino, Electron cyclotron resonanace heating and current drive in toroidal fusion plasmas, Plasma Phys. Control. Fusion **36**, 1869 (1994).

[2] H. Zohm, et al., Experiments on neoclassical tearing mode stabilization by ECCD in ASDEX Upgrade., Nucl. Fusion **39**, 577 (1999).

[3] S. Alberti, T.P. Goodman, M.A. Henderson, A. Manini, J.-M. Moret, P. Gomez, P. Blanchard, S. Coda, O. Sauter, Y. Peysson and the TCV Team, Full Absorption of third harmonic ECH in TCV tokamak plasmas in the presence of second harmonic ECCD, Nucl. Fusion **42** (2002), 42 .

[4] R.H. Cohen, Nucl. Fusion **28** (1988),1871.

[5] K. Matsuda, IEEE Trans. Plasma Sci. **PS-17** (1989),6.

[6] Y.R. Lin-Liu, et. al., in Controlled Fusion and Plasma Physics (Proc. 26th Eur. Conf. Maastricht, 1999), Vol. 23J, European Physical Society, Geneva (1999), 1245.

[7] R. Magne et. al., Very long pulse testing of the TH1506B 118 GHz Gyrotron, Proc. 14th Topical Conference on Radio Frequency Power in Plasmas, Oxnard, California (2001), 477.

[8] S. Alberti et. al., European high-power CW gyrotron development for ECRH systems, in Fusion Engeneering and Design (Proc. 11th joint Workshop on Electron Cyclotron Emission and Electron Cyclotron Heating, Oharai, Japan, 1999) **53** (2001),387–397.

[9] T.P. Goodman, S. Alberti, M.A. Henderson, A. Pochelon and M.Q. Tran,design and installation of the Electron Cyclotron Wave System for the TCV Tokamak, in Fusion Technology (Proc. 19th Symp. on Fusion Technology Lisbon, 1996), Vol. 1 (1997), 565.

[10] J.A. Murphy, Distorsion of a Simple Gaussian Beam on Reflection from off-axis Ellipsoidal Mirrors, Int. J. of IR&MM Waves, 8(9) (1987), 1165–1187.

[11] A. Manini et. al., Modulated ECH power absorption measurements using a diamagnetic loop in the TCV tokamak, Plasma Physics and Controlled Fusion, **44**(12) (2002), 139–158.

[12] S. Nowak and A. Orefice, Three-dimensional propagation and absorption of high-frequency Gaussian beams in magnetoactive plasmas, Phys. Plasmas **1**(5) (1994), 1242–1250.

# Design of the evacuated waveguide transmission lines for JET-EP.

M.A. Henderson, S. Alberti, J. Bird[1], B. Elzendoorn[2], T.P. Goodman, F. Hoekzema[2], G. MacMillan[1], B. Pioscyk[3], L. Porte, A.G.A. Verhoeven[2].

Association EURATOM-Confédération Suisse
PPB – 222, CH 1015 Lausanne, Siwtzerland
1) EURATOM-JET/UKAEA Culham
2) EURATOM/FOM-Instituut voor Plasmafysica 'Rijnhuizen'
3) EURATOM/FZK-Karlruhe

An over moded evacuated waveguide line was chosen to be used in the transmission system for the proposed JET-EP ECRH project. The system includes 6 lines of 63.5mm waveguide for transmitting the 6.0MW(10s) at 113.3GHz from the gyrotrons to the launching antenna. The lines will be on average 72m in length and consist of 9 miter bends for an estimated transmission efficiency of 91%. Each line will include an evacuated switch leading to a calorimetric load, two DC breaks, two gate valves, one pumpout Tee, a power monitor miter bend and a double disk CVD window near the torus. The location of waveguide supports will be positioned to minimize power converted to higher order modes from waveguide sagging and misalignment. The two gate valves and CVD window will be used as tritium barriers at the torus and between J1T and J1D. The last leg of the waveguide leading to the torus will be designed to accommodate for the torus movement during disruptions and thermal cycles. All lines will also be designed to be compatible for 170GHz operation. A brief description of the line and discussion of the above topics will be presented.

## I. Introduction

The JET-EP ECRH system[1] was planned to begin operation at the beginning of 2004 with the full 6.0MW available in 2005. Recently, the project has fallen victim to budget cuts and is no longer planned to be installed. The conceptual design work for the transmission line system was nearly complete at the time of cancellation. The design criteria that led to this design could be useful in the design and installation of ECRH systems on future machines such as ITER. This document provides a basic outline of the transmission line design, a full description will be available from the JET archives[2]. A brief history of the choice of transmission systems is described in part II. Part III describes the design of the transmission line as it stood at the cancellation of the project. The design of a high power microwave transmission system in an existing tokamak site encounters several hindrances from tritium handling to clearance for overhead crane passage; part IV discuss some of these problems. Application of this design to other machines is discussed in part V.

## II. Design History

Originally the transmission system for the JET-EP ECRH project had been an evacuated 63.5mm diameter corrugated waveguide (WG63). From the initial design there has been a series of alterations motivated by cost savings or potentially reduced risks of Tritium leakage from J1T to J1D. From a cost perspective the evacuated waveguide was viewed as an expensive method of transmitting the microwave power from the gyrotrons to the tokamak. In addition, there was concern that an evacuated waveguide line which traversed the barrier between J1T and J1D would pump Tritium into J1D. This motivated the design of a quasi-optical (QO) mirror system on JET-EP, which offered nearly 25% reduction in costs. Additional CVD window at the J1D-J1T barrier calmed the fears of a Tritium leak into J1D.

However, a complete QO line from Gyrotron to torus had drawbacks. Shielding around the section of the line in J1D, required to avoid stray radiation, would obstruct the use of an overhead crane.

All envisioned routings were deemed unacceptable to the JET Operator which led the design team to propose a hybrid design of an atmospheric 87mm waveguide line in J1D and a QO line in J1T. The atmospheric line prevented the pumping of Tritium from J1T to J1D and also avoided radiation leakage.

The cost estimated for the different transmission systems including all elements from the output of the Matching Optics Unit (MOU) at the gyrotron up to but not including the double disk CVD diamond window unit before the launcher. The QO line required larger diameter and thicker disks which increased the price of the CVD disks considerably. Taking into account the additional cost of the CVD windows, the price differences between the WG63, QO and WG87-QO lines were all with in ~3% of the total price. In light of this, the JET-EP ECRH team re-evaluated the two options (WG87-QO and WG63) and decided to return to an evacuated waveguide line. Along with the 63.5mm waveguide other waveguide diameters were investigated (31.75mm and 45mm), but the 63.5mm had a clear advantage; the waveguide components could be re-used on ITER. The waveguide components could be built broadband facilitating both the 113.3 GHz for JET and 170GHz for ITER. Recuperating the waveguide elements for ITER reduced the effective cost of a waveguides line by half to ~280k€ assuming the waveguides are re-used.

**III. Transmission Line Routing**

The 6 gyrotrons were to be located on the south side of the J1D building. Each gyrotron connected to a waveguide line which transmits the microwave beam to the entry port of the launching antenna at the torus in J1T. An overall view of the two buildings and the location of the different elements are shown in Figure 1. Each waveguide line leaves the MOU horizontally and travels to the east end of the gyrotron platform. A miter bends directs each waveguide downward to a level of >2.5m above the ground floor and then toward the J1T building. After passing through the barrier between J1T and J1D a third miter bend sends the beam upward at an angle to a height >7.2m above the J1T floor. The waveguide lines follow a 'dogleg' around the ventilation shaft in the south-east corner of J1T and then along the east wall opposite the port in Octant 1, see Figure 2. A 7th miter bend sends the waveguide towards the torus. A second 'dogleg' deviates the waveguide around the KN3 diagnostic and into the launching antenna's port.

Each line has a total of 9 miter bends and an average length of 72m. A typical line has a DC break at either end isolating the line from the gyrotron and torus, a pumpout Tee near the barrier in J1T, two all metal gate valves, a power monitor miter bend near the torus, a CVD window housing unit and a switching network to deviate the beam either to the torus or to a calorimetric load. The transmission efficiency of the line is estimated to be ~90.4%. The losses include an estimated 3.6%

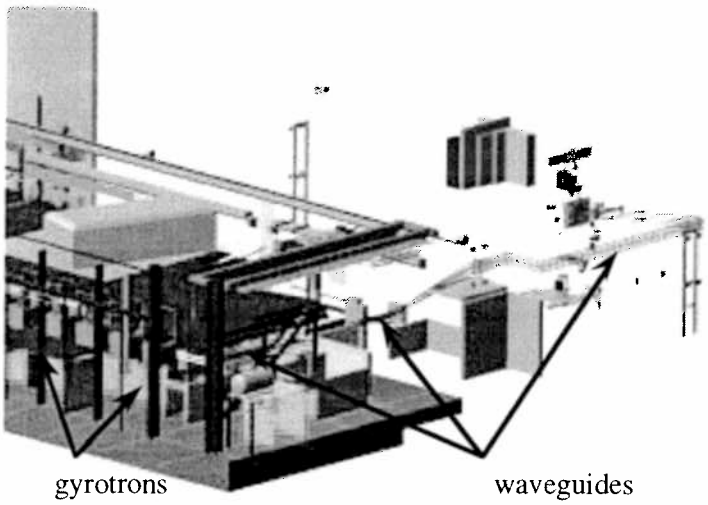


Figure 1 View of the J1D and J1T halls including the gyrotrons (bottom left), waveguide lines and input to the JET torus. The waveguide lines in J1D run eastward up to the next to the last gyrotron then drop down to a height of >2.5m above the ground floor. A miter bend directs each line toward J1T. In J1T the lines rise to a height of 7m and around to wall until opposite Octant 1 before going into the launcher

of mode impurity from coupling into the waveguide, 4.0% losses from a combination of ohmic attenuation (from waveguide and miter bends) and conversion to higher order modes (at miter bends) and 2.0% of the power converted to lower order modes either at the miter bends or due to bending of the waveguide.

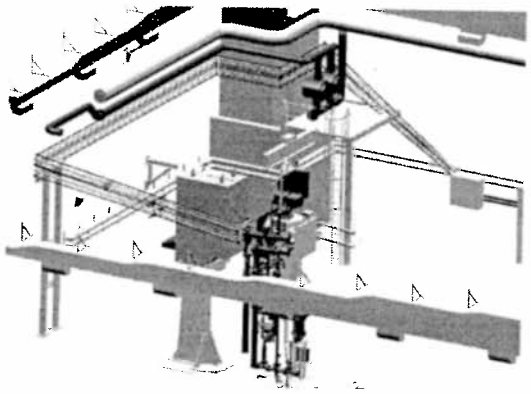

Figure 2 Waveguide run in J1T up to the entrance into the launcher port in Octant 1.

## IV. Specifics to the JET-EP transmission line.

Several criteria had to be met in the design of the waveguide line for the JET-EP project. These criteria included: no Tritium leakage from the torus via the transmission line, no neutron radiation into J1D from J1T via the waveguide passage through the wall, compensation of torus displacements due to disruptions and thermal cycles, minimization of obstructions from the transmission line, gyrotron conditioning and calibration capabilities, waveguide support locations, etc. The detailed description of these topics can be found in the design review documentation[2] of the transmission line. Only a few topics will be addressed in this text.

### Tritium Barriers

Risks associated with Tritium leakage from the torus into either J1T or J1D via the transmission line was one of the greatest concern of the JET Operator. These risks were minimized by the design team by maintaining a similar Tritium containment philosophy as that of the JET installation, two barriers: torus vessel and J1T enclosure. The first barrier at the wall of the vacuum vessel was maintained by a combination of an in-line all metal gate valve followed by a in-line double disk CVD window. The CVD window unit experienced three different vacuums, the torus vacuum on the side facing the torus, the waveguide vacuum on the side facing the gyrotron and inter-space vacuum between the two disks. All three vacuum regions were isolated from the others. The intervacuum space was monitored continuously, a change in pressure implied to a rupture of the isolation between this volume and either the torus or waveguide vacuums. In this event the security system assumed the leak came from the torus and therefore the Tritium barrier had failed (this event is referred to as a "CVD disk failure"). The gate valve at the torus would then close to eliminate the potential leak. In addition, the other in-line gate valve and the gate valves on each pumping stations would close to minimize the potentially contaminated volume, see Figure 3.

The second Tritium barrier at JET was located at the wall between J1T and J1D. The waveguide passing through this wall could be a potential leak of Tritium from J1T into J1D. In the event of a fast rupture in the CVD window, some Tritium would pass into the waveguide line before all of the gate valves closed. Most of the Tritium would be pumped via the pumpout Tee located near the J1T-J1D interface, however, some particles could continue upstream in the

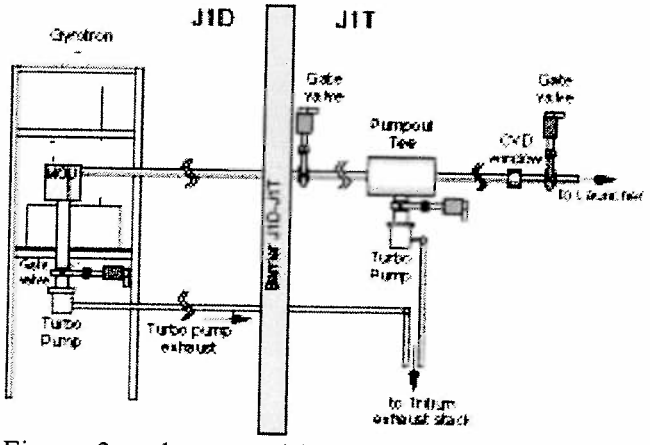


Figure 3 the two tritium barriers for the transmission line: first barrier (gate valve and window at torus) at the torus and the second (gate valve) at the J1T-J1D wall.

direction of the MOU pumping station. These particles would be blocked by an all-metal gate valve located on the inside wall between J1T and J1D. This gate valve would close in the event of a CVD disk failure. The CVD disk failure would also trigger the closing of the gate valves on all the pumping stations, which would confine the tritium to the waveguide volume. A further barrier was added in case all the gate valves failed to close, the exhaust lines of both the MOU and pumpout Tee turbo pumps were vented back into J1T and out the exhaust stack. Thus limiting the containment to the waveguide and MOU volumes.

**Gyrotron Calibration & Conditioning**

One of the requirements of the transmission line was to operate the gyrotron either into the tokamak or into a calorimetric load with the switching between the two made from remote operation. At the beginning of a day the gyrotrons would be fired for short pulses to insure the correct operating beam current. This required directing the beam into a load rather than the torus (stray microwave power in the torus would cause damage even at short pulses). Also, conditioning of the gyrotrons would be needed after long periods of down time, which required a long pulse load. To achieve both of these requirements a switching system was designed similar to the W7-X ECRH quasi-optical transmission line. A single load shared between two gyrotrons (this reduces the costs per line by ~10%) with a switch positioned near the output of each MOU, see Figure 4. Three short pulse load (~200ms) are used for daily operation. When a given gyrotron needed conditioning a single spare long pulse load could be installed (long pulsed loads cost a factor of 2.5 more).

An additional switching system was added near the torus which directs the beam either to the torus or to the its load via a return path in a neighboring line, see Figure 4. Calibration and conditioning of the transmission line to full pulse operation could be performed without having access to the J1T zone. The calibration of the line allowed a measure of the power delivered to the torus after the losses in the line, and was cross calibrated to a Power Monitor Miter Bend located just before the switching network near the torus. With this option a 3-way switch is placed near the gyrotron, directing the beam either forward, toward the load with beam coming from the gyrotron or toward the load with the beam coming from the neighboring gyrotron via the switching network near the torus.

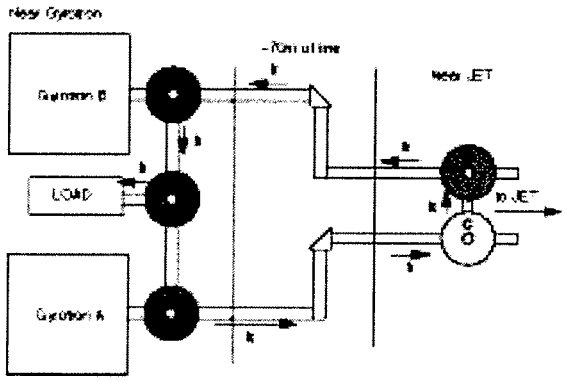


Figure 4 Schematic of the switching system for conditioning of the gyrotrons and calibration of the line in-situ. One load is shared between

**Line - Launcher Interface**

The interface between the transmission line and the launching antenna (Launcher) was complicated by the torus displacement during disruptions and thermal cycles. The launcher mounted in the port of Octant 1, moved with the torus. The transmission line had to be flexible to accommodate the movements of the torus. The outer flange of the launcher can move 8mm toroidally and 16mm radially during a disruption and 17mm radially due to thermal expansion when heating the torus. To reduce the induced stress the waveguides were aligned (unstressed) when the torus is hot, thus the maximum radially displacements were ± 16mm (disruption) or -17mm (cooled torus) but never the addition of the two displacements simultaneously.

The section of the transmission line near the torus is shown in Figure 5. The CVD window units were fixed to the launcher flange, avoiding breaking the CVD diamond disks from the bending stresses. The length of waveguide between the CVD window and the nearest support was >2.5m, which allowed for bending of the waveguide during the displacement. The waveguide leg #9 was >1.2m in length, the induced stress from the 17mm displacement was less than 80% of the Yield Strength for the Aluminum waveguide. The 8mm toroidal expansion was accommodated with the waveguide leg #8 which will be >1.0m in length before the next support.

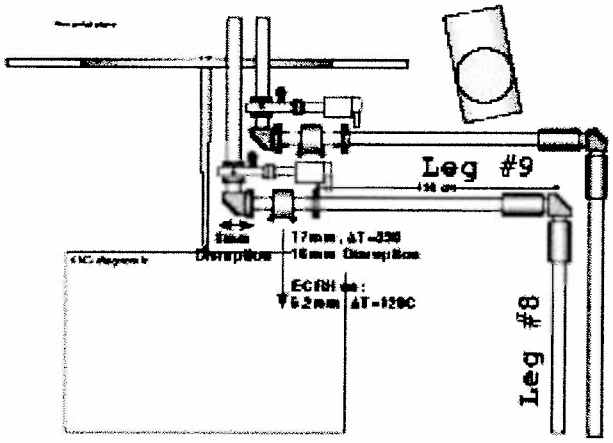


Figure 5 The waveguide legs #8 and 9 bend slightly to compensate for the torus displacement due to disruptions and thermal cycles.

Of the 8 launching antennas for the JET-EP launcher 2 were spares which could be used in the event one of the other antennas failed or if an ITER 170GHz gyrotron was installed. In the event of a launcher failure, the waveguide lines leading up to the torus would be modified to connect a given gyrotron to a new antenna, see Figure 6. The gate valve before the torus would be closed and the line(s) would be remounted. Pumping the region between the gate valve and the CVD window was made via a pumping port on the gate valve. The changing of launcher would require human intervention into the J1T zone, lasting about one day.

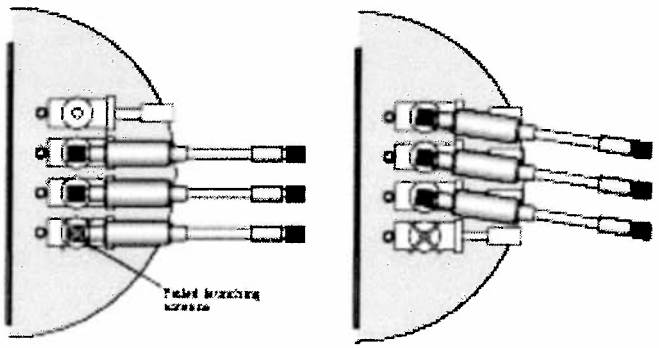

Figure 6 The waveguide leg #9 can be modified to reconnect the gyrotron to a new launcher in case a given launcher fails (worse case shown).

**Waveguide supports**

The supports used for the waveguide sections and the alignment procedures would be similar to those used in mounting and aligning the transmission line for the TCV tokamak[3]. A precision of ~ 1mm between supports can be achieved using a simple laser which placed co-axially with the output of a miter bend section. The laser beam provides a reference for positioning the next miter bend and supports along this path. The spacing of the supports was chosen by minimizing the power converted to other modes due to misalignments and waveguide sagging. Small distances between supports created a high level of mode converted power from small misalignments while large distances between supports created a high level of mode converted power from the sagging of the waveguide due to gravity. A typical line of 72m in length was investigated to determine the optimum range for the distances between supports. As a first step the total power converted to all higher order modes at the end of the line was calculated for spacing between supports, the spacing was kept constant over the entire length of the line. For the same spacing the power converted due to a 1mm shift between two supports was

calculated and then multiplied by the number of supports used in the line, see Figure 7. The addition of these two losses yielded a minimum in converted power for support spacings between 4 and 6m. The support spacings of 3.5m and 7m would be avoided, these lengths correspond to a beat wavelength between the fundamental and a higher order mode. The estimated power losses for the misalignment and waveguide sagging provides an upper bound on the power converted to other modes, in practice the lengths between supports would have been varied along the length of the transmission line and the misalingment error would vary between +1mm to -1mm. The next step, had the project continued, was to determine the possible support locations available at the JET site and optimize the choice based on the minimum amount of converted power to other modes.

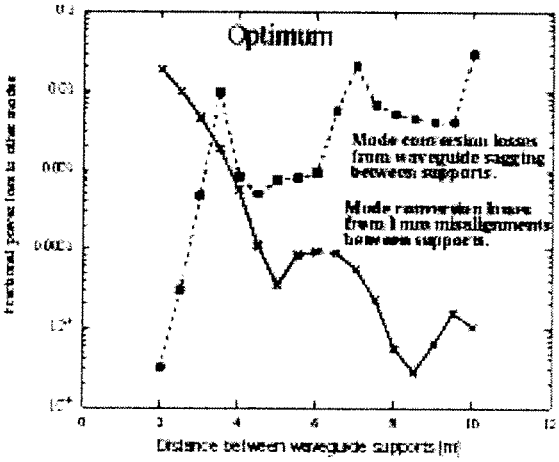


Figure 7 Fractional power converted to higher order modes from sagging and misalignment of the waveguide versus the distances between supports. The sum of the two curves has a minimum for support spacings between 4 to 6m.

## V. Conclusion

Preliminary comparisons of the different transmission line systems (quasi-optical, atmospheric and evacuated waveguide lines) lead to the conclusion that the cost differences between the various transmission systems were negligible. The final transmission system chosen for JET-EP was the 63.5mm evacuated waveguide which offered compactness, high transmission efficiency and security from Tritium leakage and microwave radiation with out additional costs compared to a hybrid atmospheric waveguide - quasi-optical transmission line.

Despite the demise of the JET-EP ECRH project, the design study of the transmission line system has been a useful exercise which may prove beneficial in the design and construction of future devices with high power microwave heating systems. The Tritium containment philosophy used in this study offers a reliable system which could be used as the basis for the ITER design. Likewise, the novel switching system which allows conditioning and calibration of the entire system without human intervention can easily be applied to the ITER ECRH system.

## Acknowledgements

The author would like to thank the many people at JET who were very helpful in answering the numerous questions asked in an attempt to make the transmission line compatible with the JET site.

This work was partly supported by the Swiss National Science Foundation

## References

1) A.G.A. Verhoeven et al 2001 The ECRH System for JET, this conference.

2) JET EP-ECH-TLR-R-001: General description of the Evacuated Waveguide Transmission Line for the JET-EP ECRH Project (in preparartion)

3) T.P. Goodman et al 1996 Proc. of the 19th Symposium on Fusion Technology, Lisbon p.565.

Supplement to LRP 726/02
EC-12 Workshop, Aix-en-Provence, May 2002

# Summary of the ECRH/ECCD Experiments Sessions of the EC-12

T.P. Goodman
*Centre de Recherches en Physique des Plasmas,*
*Association EURATOM-Confédération Suisse, EPFL, 1015 Lausanne, Switzerland.*

Twelve talks and 26 posters were presented during the experimental sessions of the EC-12 conference. The tokamak, stellarator, reverse field pinch (RFP) and mirror trap geometries were discussed.

## *EBW*

The most significant change in the conference over previous years was in the number of presentations concerning the electron Bernstein wave (EBW) schemes of emission (E), heating (H) and current drive (CD). This reflects the need for heating schemes in high density spherical toakamak experiments, in particular. Also new, were experiments using gyrotrons for high density heating of simple mirror traps (Zorin, Vodopyanov). EBE is covered in the ECE summary and the theoretical background is given in the theory summary. Ray-tracing for these waves, even in the 3-D geometry of the stellarators (Nagasaki), was carried out. EBH provides a possible explanation for heating in Heliotron J when no electromagnetic resonance is present in the core (Nagasaki). O-X-B heating was shown on W7-AS (Laqua) at 2$^{nd}$, 3$^{rd}$ and 4$^{th}$ harmonics using 140GHz. The strong variation of $n_{//}$ (first noted by Forrest) was highlighted by a number of investigators. In particular, EBCD was measured in W7-AS (Laqua) using 70GHz and inferred from loop voltage measurements. In Compass-D (Shevchenko) direct HFS launch of the slow X wave led to mode conversion to the EBW at the upper hybrid layer, below the tokamak midplane. A toroidal injection angle scan clearly shows that the loop voltage change was largest at *perpendicular* injection – in contrast to X-mode current drive expectations but in agreement with EBW ray-tracing and Fokker-Planck calculations. The inferred driven current amounted to more that 100kA counter current drive. When scaled with power, $n_{//}$, major radius R, electron temperature $T_e$ and density $n_e$, this current is comparable to the 1.2kA current measurements of W7-AS. The normalized current drive efficiency of $\eta_{20}=ne_{20}RI/P\sim0.034$ (A/W $10^{20}$ m$^{-2}$) was found for EBCD on Compass-D which compares favorably with typical ECCD efficiencies. It was pointed out (Laqua) that the resonance curves are changed from ellipses (ECCD) to hyperbolas (EBCD) as $n_{//} > 1$ and can therefore lead to efficiency similar to lower hybrid current drive.

## *MECH*

ECH physics studies were carried out on Asdex-Upgrade (Leuterer) and FTU (Cirant, Jacchia) in which modulated ECH (MECH) was used to study electron heat transport. Asdex-Upgrade reported a multi-machine critical value $R/L_{Te} \sim 10$ for what has been called the stiff region of the electron temperature. It was also shown that a step change in transport occurs when the critical temperature scale length, $L_{Te}$, is exceeded. Using MECH both on– and off–axis, regions of low and high, energy transport were probed. The step behaviour is well described quantitatively by the Weiland physics-based model (transport by trapped electron modes (TEM)). FTU showed that the location of the change in transport was neither the deposition location nor the inversion radius. MECH on FTU evidenced the change from low to high heat flux on a fast time scale and proportionality of the critical $R/L_{Te}$ on s/q.
MECH was used on TCV (Manini) to measure ~50% absorbed power (on an Ohmic target) of the 3$^{rd}$ harmonic (X3) ECH; launched for the first time from the top of the

tokamak (Hogge). This is in good agreement with linear theory. The measurement used the modulated response of the diamagnetic loop (DML) and required careful compensation of the vessel image currents. The DML and $T_e$–profile changes at the shutoff of ECH were used in the L-2M Stellarator (Akulina) to measure ~75% power absorption with good agreement between the two methods. TORE SUPRA (Zou) also found good agreement between measured and calculated power absorption. TJ-II (Fernandez) measured deposition profiles using MECH which were wider than calculated by ray-tracing as has been reported in the past, on other machines. Finally, of importance for future feedback schemes, the deposition location could also be tracked, using MECH, during scans of toroidal field in FTU (Cirant).

***NTM stabilization with consequent performance enhancement***

Performance improving 3/2 neoclassical tearing mode (NTM) stabilization was reported for DIII-D (Prater) and Asdex Upgrade (Leuterer). A 60-70% increase in $\beta$ was shown; however, feedback/tracking needs to be implemented (DIII-D) due to the Shafranov shift and accompanying resonance surface motion when $\beta$ increases, for the particular inboard absorption location used in both machines. DIII-D has implemented a seek-and-dwell technique to match the deposition to the resonant surface, using either plasma motion or magnetic field adjustment with Mirnov coils providing the control signals.

Considering the importance of ECCD on ITER, NTM stabilization experiments are needed in which deposition tracking (shown: FTU) and resonant surface tracking (e.g. via fast equilibrium reconstruction (DIII-D)) are combined with fully *external* actuators (i.e. mirrors). Stabilizing a mode during it's growth phase, would be an interesting demonstration. The driven current at the resonance surface required for stabilization, must be measured to allow comparison with NTM theory. This requires full power accounting (e.g. spurious 3$^{rd}$ harmonic absorption, X/O mode ratio, etc.) and multiple launcher alignment in order to be relevant to the ITER design. Careful power accounting on DIII-D (Lohr), at least from the gyrotron to the plasma, has been carried out. As an example, 2/1 stabilization on DIII-D (Prater) is expected to require 5 gryotrons, instead of the 4 gyrotrons used at present. The uncertainty in the *local* absorbed power is often of the order of ~25%. On the other hand, a large database of ECCD shots from DIII-D was compiled to show that FP calculations are in excellent agreement with experimental measurements of the driven current on DIII-D (Prater). [However, see comparisons with TCV (Harvey, Nikkola)]. It should be noted that present techniques for alignment are in-vessel and/or shot intensive.

***Extension of operational domains***

*eITBs*

Off-axis ECCD was used in TCV (Nikkola) and JT-60U (Ikeda) to produce reversed or flat-shear profiles exhibiting electron internal transport barriers (eITB). In TCV, fully-sustained steady-state reversed-shear was achieved with off-axis co-ECCD. The bootstrap fraction of ~50% was responsible for the reversed shear (RS) as the ECCD current profile was expected to be flat due to radial diffusion of the current, modeled by the Fokker-Planck (FP) code CQL3D. Proper amounts of additional cnt-ECCD inside the barrier enhanced the hollowness of the current profile and evidenced the steady-state barrier. In other machines the ITB is transient on current diffusion time scales but steady state on energy confinement time scales and is often produced during current ramp-up assisted by other heating methods (e.g. LH on FTU,

Granucci). With EC injection *after* the Ip ramp, JT-60U measured flat (off-axis ECCD) and strongly RS (on-axis ECCD) q-profiles with the foot of the ITB at $q_{min}$ for both off-axis and near on-axis ECCD. FP calculations of ECCD were consistent with MSE measurements except with truly on-axis ECCD. For on-axis ECCD either after or during the current ramp, MSE suggested a "current hole", while FP-calculated ECCD was large on-axis. As $q_{min}$ decreased, the Te inversion location moved inward. In TEXTOR (Westerhof) the "q-comb" model for $\chi_e$ was used to describe the electron transport barrier seen in Thomson scattering measurements, as in RTP. The barrier appears near q=1. Further evidence of the importance of low order rational q-surfaces (q=1) to the electron temperature was shown on TJ-II (de La Luna) during periodic modification of the iota-profile by external currents. LHD (Shimozuma) also reported high electron temperatures, improved confinement in the core, and a power threshold which increases with increasing density.

*Sawtooth stabilization*

TEXTOR (Westerhof) showed sawtooth stabilization *outside* of the inversion radius as in AUG, FTU and TCV, in accordance with theory. AUG investigated stabilization with ECH, Co- and Counter-ECCD, showing several regions of stabilization depending on the method used.

*Confinement scaling*

JT-60U, TCV and TEXTOR reported $P_{EC}^{a}$ ($0>a\leq1$) scaling with EC power inside the ITB (JT-60U & TCV) and during the RI-mode (TEXTOR: Westerhof).

*High elongation*

Far-off axis ($\rho$ ~0..7) ECH and ECCD was used on TCV (Camenen) to allow operation at low normalized current $I_N$ and high elongation ($\kappa$ ~2.4) while maintaining vertical stability; in preparation for $\beta$-limit studies using central X3 heating.

*Current profile control*

Finally, DIII-D (Lohr) has moved one step further along the road (taken initially by RTP; e.g. EC-10, 11) to control of plasma performance. By implementing temperature feedback control, using ECE measurements in a control loop acting on the gyrotron acceleration voltage, the current ramp-up has been controlled, in preparation for AT experiments.